Electronic Supplementary Material (ESI) for Green Chemistry.

Supplementary information

From silicon to silicones without dimethyldichlorosilane. Green Direct mechanochemical synthesis of methylmethoxysilanes from silicon and dimethyl ether (DME).

I.N. Kryzhanovskii[1,2], M.N. Temnikov[1,2*], A.A. Anisimov[1,2,3], A.K. Ratnikov[1,2,3], I.V. Frank[1,3] A.V. Naumkin[1], S.M. Chistovalov[1,2], and A.M. Muzafarov[1,4].

[1]*A. N. Nesmeyanov Institute of Organoelement Compounds, Russian Academy of Sciences, 119334, Moscow, Russia*

[2]*Tula State Pedagogical University. L.N. Tolstoy, 300026, Tula, Russia.*

[3]*Moscow Institute of Physics and Technology (National Research University), 117303, Dolgoprudny, Moscow Region, Russia*

[4]*Enikolopov Institute of Synthetic Polymeric Materials, Russian Academy of Sciences, 117393, Moscow, Russia*

E mail: temnikov88@gmail.com

Contents

1. Common information and methods 4

1.1. Materials 4

1.2. Methods and analysis 4

1.2.1. NMR 4

1.2.2. Gas chromatography analysis (GC) 4

1.2.3. Powder X-ray diffraction (PXRD) 4

1.2.4. Scanning electron microscopy (SEM) 5

1.2.5. X-Ray photoelectron spectroscopy (XPS) 5

1.2.6. Fourier-transform infrared spectroscopy (FTIR) 5

1.2.7. GPC 6

1.2.8. Gas chromatography-mass spectrometry analysis (GC-MS) 6

1.3. Experimental 6

1.3.1. Typical experiment with copper (I) chloride as a source of copper 6

1.3.2. Typical experiment with copper as a source of copper 7

1.4. Calculations 9

2. XPS elemental analyses 11

3. Spectra and other additional information 12

3.1. SEM-EDX – images and spectra....12
3.2. PXRD – data....19
3.3. XPS – spectra, tables and description....20
3.4. NMR....31
3.5. GC-MS analysis....40
3.6. GC....42
3.7. GPC....44
3.8. FTIR....45
4. References....47

1. Common information and methods

1.1. Materials

Technical grade silicon KR-1 (1-1.5 mm, purity > 98%, major impurities Fe < 0.7%, Al < 0.7, and Ca < 0.6%) was used as the source of silicon. Commercial CuCl and Cu powder (3 μm) were used as the copper catalysts. Commercial Zn powder was used as additive. Commercial Sn powder was used as additive. CuCl was purchased from ABCR. Cu powder was purchased from Sigma-Aldrich. Sn powder and Zn powder were purchased from Omega Snab Complect. Dimethyl ether was purchased from Sigma Aldrich.

1.2. Methods and analysis

1.2.1. NMR

^{1}H, and ^{29}Si NMR spectra were recorded on a Bruker Avance™ 500 and Bruker Avance™ 600 spectrometers (Germany) (at 500.13 and 600.22, 99.36 MHz for 1H and 29Si, respectively). The ^{1}H chemical shifts were measured relative to TMS using residual signal of solvent $CDCl_3$ (7.26 ppm). The ^{29}Si NMR spectra were measured in $CDCl_3$ containing $Cr(acac)_3$ (30 mmol/L). The ^{29}Si chemical shifts were measured relative to TMS used as the external standard.

1.2.2. Gas chromatography analysis (GC)

Gas chromatography (GC) analysis was performed on a Cromatec Crystal 5000 chromatograph (Russia) at 50–250 °C, 20° min^{-1}; catharometer detector, columns (2 mm × 2 m) with 5% SE-30 stationary phase deposited onto Chromaton-N-AW-HMDS, helium as a carrier gas (20 mL min^{-1}). Data were recorded and processed using the Chromatec Analytic program package (Chromatec, Russia).

1.2.3. Powder X-ray diffraction (PXRD)

XRD patterns were performed on a Proto AXRD θ-2θ diffractometer with a copper anode, a nickel Kβ filter (Kα=1.541874 Å) and a Dectris Mythen 1K 1D detector in the Bragg-Brentano geometry in the angular range of 20°–100° with a step of 0.02° along the angle 2θ.

Qualitative phase analysis was performed using Crystallography Open Database and the ICDD PDF-2.

1.2.4. Scanning electron microscopy (SEM)

The surface morphology was studied by scanning electron microscopy using a JSM-6000 PLUS scanning electron microscope (JEOL, Japan). The studied samples were dispersed as powders on a conducting carbon adhesive tape. The elemental composition of each surface was determined using an EX-230**BU system with integrated energy dispersive analysis.

1.2.5. X-Ray photoelectron spectroscopy (XPS)

X-Ray photoelectron spectroscopy (XPS) was carried out on an Axis Ultra DLD spectrometer (Kratos) using monochromatic Al Kα radiation with an X-ray beam power of 150 W. Survey spectra and high-resolution spectra were recorded at pass energies of 160 and 40 eV, respectively. Survey spectra were recorded with a step of 1 eV, while high-resolution spectra were recorded with a step of 0.1 eV. The dimensions of the explored area were 300 × 700 μm^2. Samples were mounted on a holder using a double-sided adhesive tape and studied at room temperature at the residual pressure in the spectrometer chamber no higher than 10^{-8} Torr. The energy scale of the spectrometer was calibrated according to the standard procedure based on the following binding energies: 932.62, 368.21 and 83.96 eV for Cu $2p_{3/2}$, Ag $3d_{5/2}$, and Au $4f_{7/2}$, respectively. To eliminate the effect of sample charging, the spectra were recorded using a neutralizer. Surface charging was taken into account based on the Si $2p_{3/2}$ peak of the Si(0) state with a binding energy of 99.34 eV.[1] The background due to electron inelastic energy losses was subtracted by the Shirley method. Quantification was performed using atomic sensitivity factors included in the software of the spectrometer.

1.2.6. Fourier-transform infrared spectroscopy (FTIR)

IR spectra were recorded on an IR spectrometer with a Fourier transformer Shimadzu IRTracer-100. Infrared spectra were obtained by liquid film method. Gas-phase IR spectrum were recorded in IR gas cell with KBr windows.

1.2.7. GPC

GPC analysis was performed on the "Shimadzu" (Japan, Germany), the detector - refractometer RID – 20 Å, the column – Phenogel 5u 500Å (Size (300 x 7,8 mm)); standart – polystyrene, eluent – toluene, THF; temperature - 40°C; speed of flow 1ml/sec.

1.2.8. Gas chromatography-mass spectrometry analysis (GC-MS)

GC-MS measurements were performed using Shimadzu QP2020 gas chromatograph-mass spectrometer with the following parameters: column: Shimadzu SH-Rtx-5MS (30 m × 0.25 mm × 0.25 μm); oven temperature: 50 °C, hold for 3 min, ramp to 200 °C at 30 °C/min, hold for 11 min; injection temperature: 250 °C; splitting ratio: split 1:10; MS ion source temperature: 200 °C; interface temperature: 250 °C; total run time: 20 min. Solvent cut-off time was 2 minutes for diethyl ether and 5 minutes for decane.

1.3. Experimental

1.3.1. Typical experiment with copper (I) chloride as a source of copper

The design and parameters of the MCHPR that was used in the direct synthesis were described in our previous work[2] and in fig. S1. Commercial grade KR-1 silicon (particle size 1-1.5 mm, 0.5 g, 17.8 mmol), copper(I) chloride (0.1 g), Zn powder (0.02 g), Sn powder (0.03 g) and ZrO_2 (stabilized with Y_2O_3) milling bodies (14 pcs, 38.38 g) were loaded into the autoclave. Then the autoclave was filled with required amount of dimethylether under chill-down using an INFLOW mass flow meter (Bronkhorst, Netherlands). The reactors with attached electric heaters were mounted in cradles. After that, autoclave heated up for 10 minutes (the temperature setting was 250°C) and then vibration drive was activated. The vibrational acceleration was 19 g. The silicon particles were ground up and stirred with a copper source by vibration milling. The resulting particles reacted with dimethylether to give methoxysilanes. After the specified amount of time of simultaneous heating and vibration, the mixture was cooled to room temperature. The liquid reaction products were analyzed by GC (see fig. S28), GC-MS (see 4.5), NMR (see 4.4) and FTIR (see fig. S30). The contact mass was separated from the reaction products by centrifugation, then washed three time with hexane, dried and studied using SEM-EDX, XPS, and PXRD.

1.3.2. Typical experiment with copper as a source of copper

The design and parameters of the MCHPR that was used in the direct synthesis were described in our previous work [2] and in fig. S1. Commercial grade KR-1 silicon (particle size 1-1.5 mm, 0.5 g, 17.8 mmol), copper powder (0.128 g), Sn powder (0.03 g), Zn powder (0.02 g) and ZrO_2 (stabilized with Y_2O_3) milling bodies (14 pcs, 38.38 g) were loaded into the autoclave. Then the autoclave was filled with required amount of dimethylether under chill-down using an INFLOW mass flow meter (Bronkhorst, Netherlands). The reactors with attached micanite heaters were mounted in cradles. After that, autoclave heated up for 10 minutes (the temperature setting was 250°C) and then vibration drive was activated. The vibrational acceleration was 19 g. The silicon particles were ground up and stirred with a copper source by vibration milling. The resulting particles reacted with dimethylether to give methoxysilanes. After the specified amount of time of simultaneous heating and vibration, the mixture was cooled to room temperature. The liquid reaction products were extracted with diethyl ether and then were analyzed by GC and GC-MS (see Figure S28).

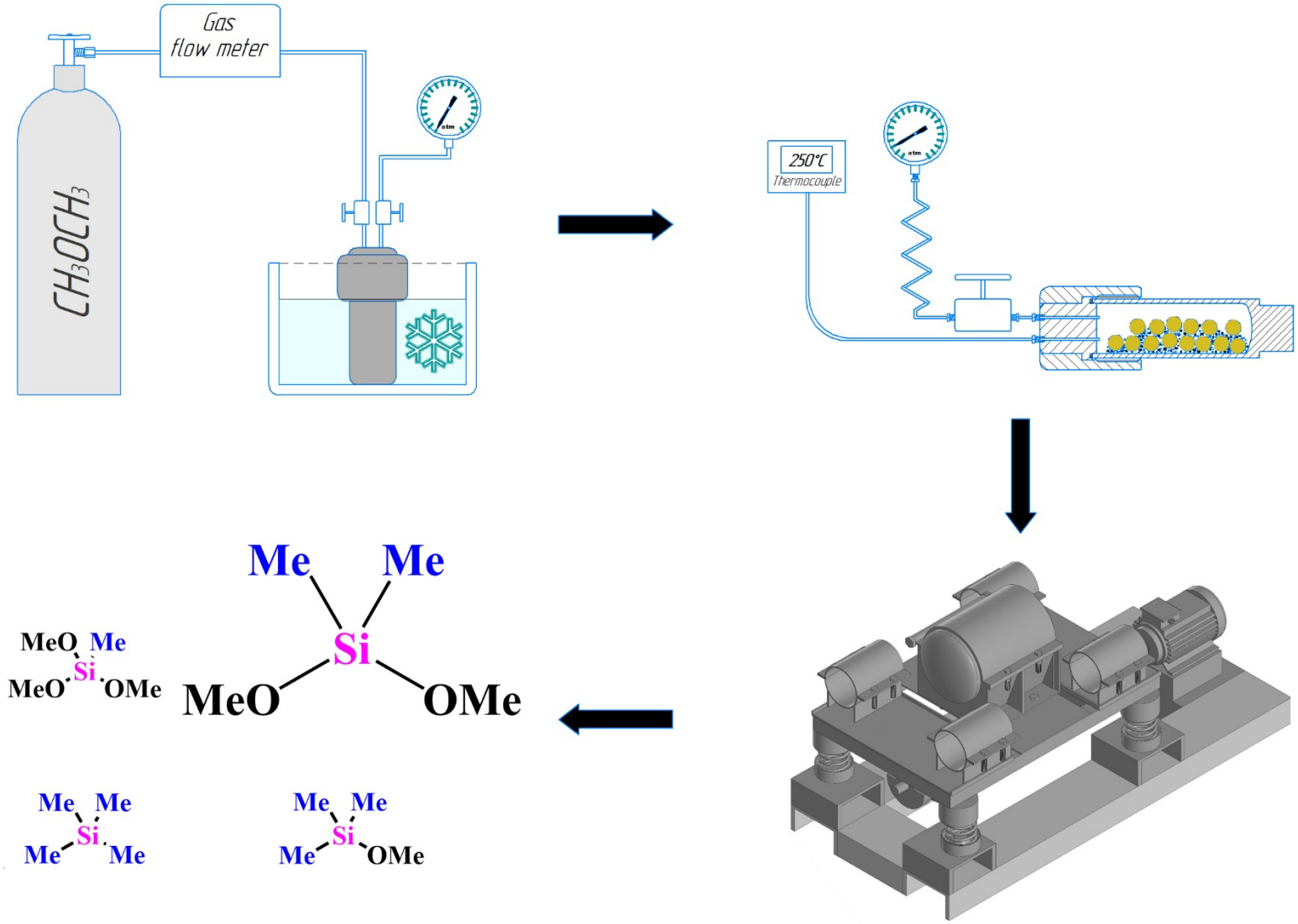

Figure S1. Experimental scheme.

1.4. Calculations

The silicon conversion and selectivity of products were estimated as follows:

Concentration data obtained with GLC give us mass relations between components of the reaction mixture. It allows us to determine the selectivities of components (S_i) by this equation:

$$S_i = \frac{W_i}{\sum W_i}$$

To determine Si conversion, we need to calculate the mass of reaction mixture.

$m_{mix} = m_{dimethylether} + m_{silicone} * C_{silicone} - m_{gas}$

m_{gas} – mass of gaseous products, mostly CH_3OCH_3. $m_{dimethylether}$ and $m_{silicone}$ are 3.3 and 1 g respectively. $C_{silicone}$ is the Si conversion.

$m_{mix} = m_{methanol} + m_{silicone} * C_{silicone} = 3.3 + C_{silicone} - m_{gas}$

$$C_{silicone} = \frac{n_{reacted\ Si}}{n_{loaded\ Si}} = \frac{\sum \frac{W_i * m_{mix}}{M_i}}{\frac{m_{silicone}}{M_{Si}}}$$

After some iterations, we get an appropriate silicon conversion.

SEM-EDX elemental analyses

Table S1. SEM-EDX elemental analyses data table (% wt).

Sample	Area	Elements (% wt)										
		Si	Cu	C	O	Al	Cl	Fe	Cr	Zn	Zr	Sn
CM-20	Reacted	72,06	0,38	19,78	5,47	0,34	0,26			0,37		1,36
	Non reacted	81,17	0,22	14,82	1,69	0,32	0,04			0,08		1,66
CM-60	Reacted	53,48	6,30	13,33	24,84	0,29	0,40	0,38		0,09		0,89
	Non reacted	88,62	0,95	4,79	3,41	0,46	0,19			0,06		1,52
CM-120	Reacted	52,26	7,19	20,74	15,18	0,49	0,72	0,72	0,23	1,31	0,44	0,71
	Non reacted	63,52	1,09	21,82	11,60	0,30	0,22				0,35	1,10
CM-240	Reacted	19,66	11,66	11,42	36,10	0,89	4,44	4,38	1,55	4,71	4,30	0,89

Table S2. SEM-EDX elemental analyses data table (% at)

Sample	Area	Elements (% at)										
		Si	Cu	C	O	Al	Cl	Fe	Cr	Zn	Zr	Sn
CM-20	Reacted	55,81	0,13	35,82	7,44	0,27	0,16			0,12		0,25
	Non reacted	67,82	0,08	28,96	2,48	0,28	0,03			0,03		0,33
CM-60	Reacted	40,48	2,11	23,59	33,01	0,23	0,24	0,14		0,03		0,16
	Non reacted	82,63	0,39	10,45	5,58	0,45	0,14			0,03		0,34
CM-120	Reacted	39,29	2,39	36,46	20,03	0,38	0,43	0,27	0,09	0,42	0,10	0,13
	Non reacted	46,62	0,35	37,45	14,95	0,23	0,13				0,08	0,19
CM-240	Reacted	15,61	4,09	21,20	50,33	0,74	2,79	1,75	0,67	1,61	1,05	0,17

2. XPS elemental analyses

Table S3. Concentrations of elements on the surface of the studied samples (atom. %), calculated from the survey XPS spectra.

Spent mass	Elements, at%								
	C	O	Si	Cu	Zn	Sn	Fe	Cl	N
CM-20	34.2	33.0	26.9	0.3	1.7	0.3	0.4	3.2	
CM-60	32.6	28.5	34.7	0.2	0.5	0.1	0.4	2.5	0.5
CM-120	36.0	33.5	27.1	0.4	0.7	0.2	0.5	1.5	0.4
CM-240	46.0	31.6	17.5	0.3	1.2	0.1	0.8	2.5	

Table S4. Concentrations of elements on the surface of the studied samples (atom. %), Calculated from the high-resolution XPS spectra.

Spent mass	Elements, at%						
	C	O	Si	Cu	Zn	Sn	Cl
CM-20	55,0	34,0	30,0	0,3	1,5	0,3	3,4
CM-60	32,5	26,9	38,0	0,2	0,5	0,1	1,9
CM-120	36,2	31,3	29,7	0,4	0,6	0,2	1,8
CM-240	45,8	29,9	20,2	0,3	1,1	0,1	2,7

3. Spectra and other additional information

3.1. SEM-EDX – images and spectra

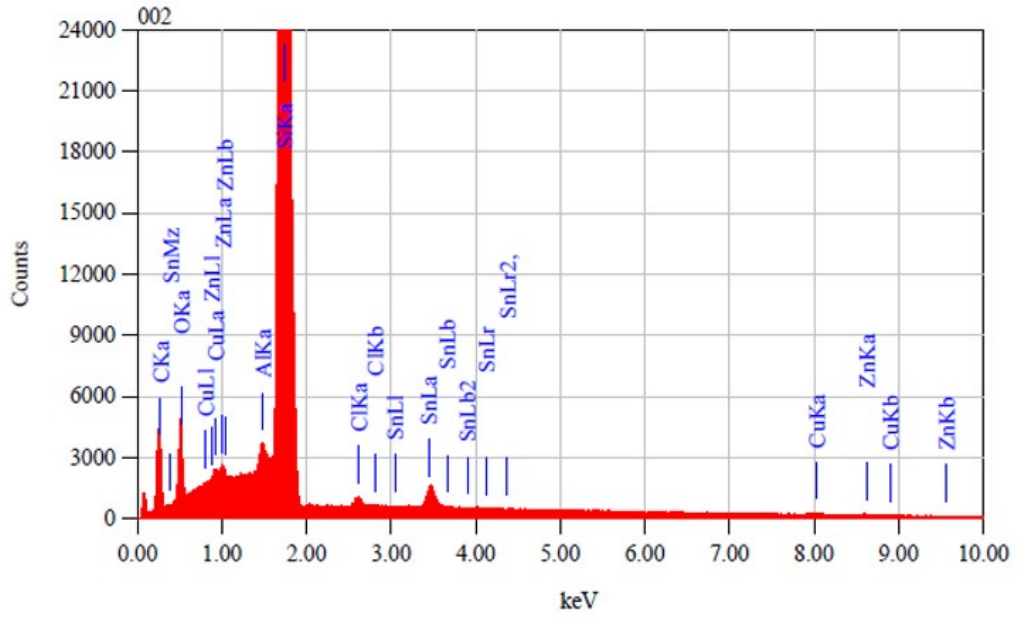

ZAF Method Standardless Quantitative Analysis
Fitting Coefficient : 0.2170

Element	(keV)	Mass%	Sigma	Atom%	Compound	Mass%	Cation	K
C K	0.277	19.78	0.09	35.82				1.4607
O K	0.525	5.47	0.04	7.44				2.6023
Al K	1.486	0.34	0.01	0.27				0.4163
Si K	1.739	72.06	0.08	55.81				93.2677
Cl K	2.621	0.26	0.01	0.16				0.2530
Cu K	8.040	0.38	0.03	0.13				0.4126
Zn K	8.630	0.37	0.03	0.12				0.3976
Sn L	3.442	1.36	0.03	0.25				1.1899
Total		100.00		100.00				

Acquisition Parameter
Instrument : JCM-6000PLUS
Acc. Voltage : 15.0 kV
Probe Current: 1.00000 nA
PHA mode : Standard
Real Time : 200.00 sec
Live Time : 144.20 sec
Dead Time : 27 %
Counting Rate: 22310 cps
Energy Range : 0 - 20 keV

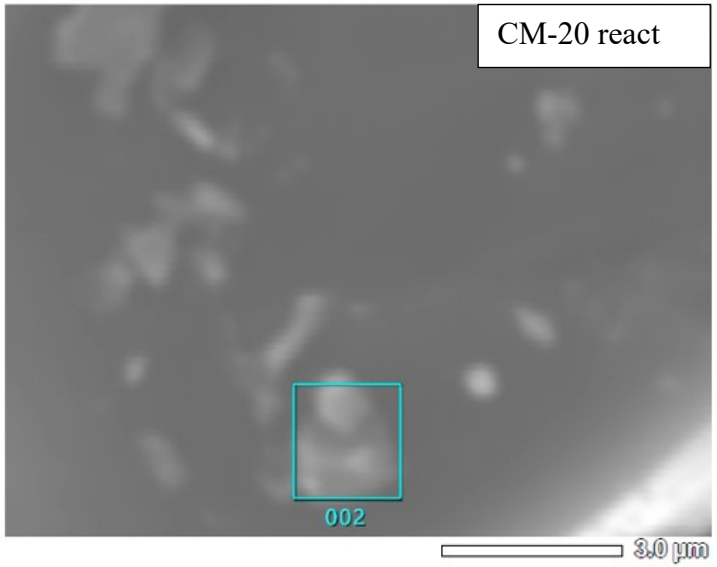

Figure S2. CM-20 reacted area.

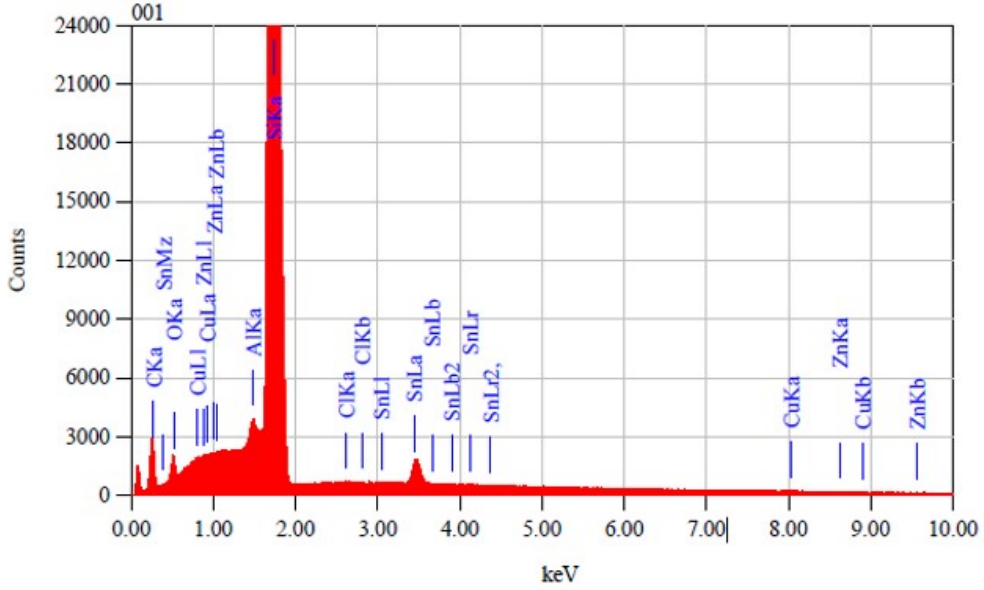

ZAF Method Standardless Quantitative Analysis
Fitting Coefficient : 0.2164

Element	(keV)	Mass%	Sigma	Atom%	Compound	Mass%	Cation	K
C K	0.277	14.82	0.08	28.96				0.8798
O K	0.525	1.69	0.03	2.48				0.7335
Al K	1.486	0.32	0.01	0.28				0.3706
Si K	1.739	81.17	0.08	67.82				96.4007
Cl K	2.621	0.04	0.01	0.03				0.0360
Cu K	8.040	0.22	0.03	0.08				0.2196
Zn K	8.630	0.08	0.03	0.03				0.0759
Sn L	3.442	1.66	0.03	0.33				1.2838
Total		100.00		100.00				

Acquisition Parameter
Instrument : JCM-6000PLUS
Acc. Voltage : 15.0 kV
Probe Current: 1.00000 nA
PHA mode : Standard
Real Time : 200.00 sec
Live Time : 138.80 sec
Dead Time : 30 %
Counting Rate: 25097 cps
Energy Range : 0 - 20 keV

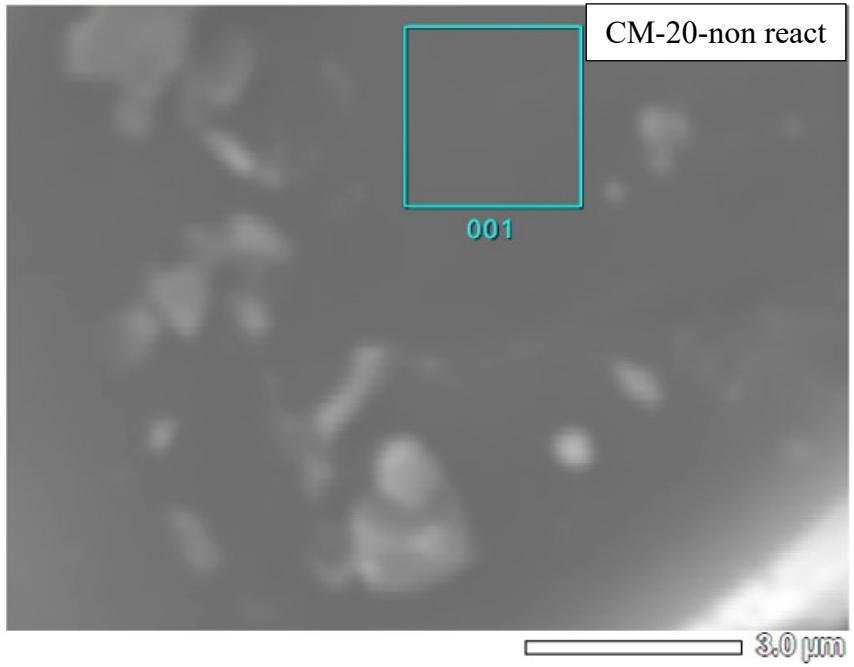

Figure S3. CM-20 non reacted area.

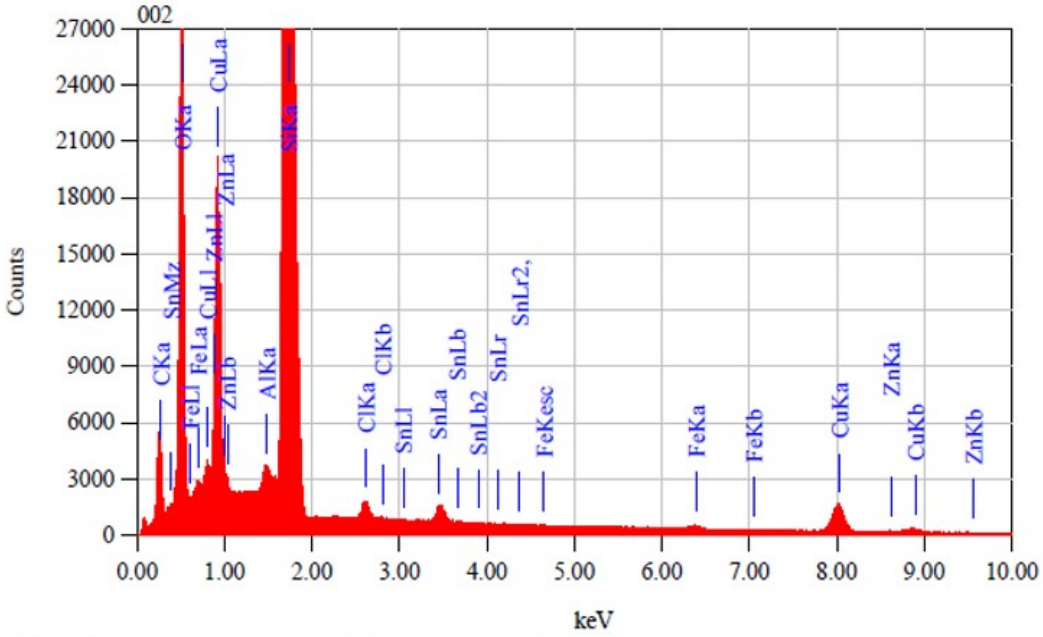

ZAF Method Standardless Quantitative Analysis
Fitting Coefficient : 0.2255

Element	(keV)	Mass%	Sigma	Atom%	Compound	Mass%	Cation	K
C K	0.277	13.33	0.06	23.59				1.5178
O K	0.525	24.84	0.07	33.01				17.6376
Al K	1.486	0.29	0.01	0.23				0.3432
Si K*	1.739	53.48	0.06	40.48				70.5896
Cl K	2.621	0.40	0.01	0.24				0.4780
Fe K*	6.398	0.38	0.01	0.14				0.5016
Cu K	8.040	6.30	0.07	2.11				7.9075
Zn K	8.630	0.09	0.03	0.03				0.1073
Sn L	3.442	0.89	0.02	0.16				0.9174
Total		100.00		100.00				

Acquisition Parameter
Instrument : JCM-6000PLUS
Acc. Voltage : 15.0 kV
Probe Current: 1.00000 nA
PHA mode : Standard
Real Time : 200.00 sec
Live Time : 139.66 sec
Dead Time : 29 %
Counting Rate: 24285 cps
Energy Range : 0 - 20 keV

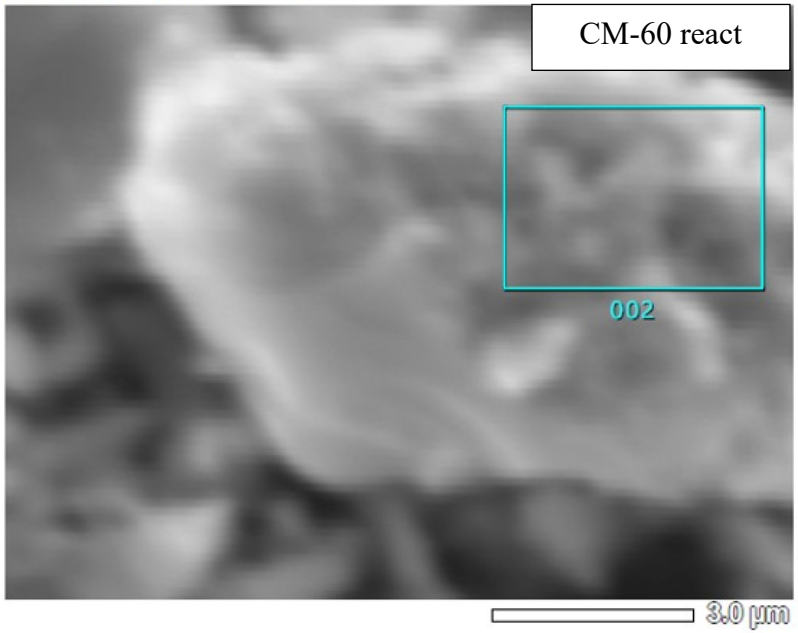

Figure S4. CM-60 reacted area.

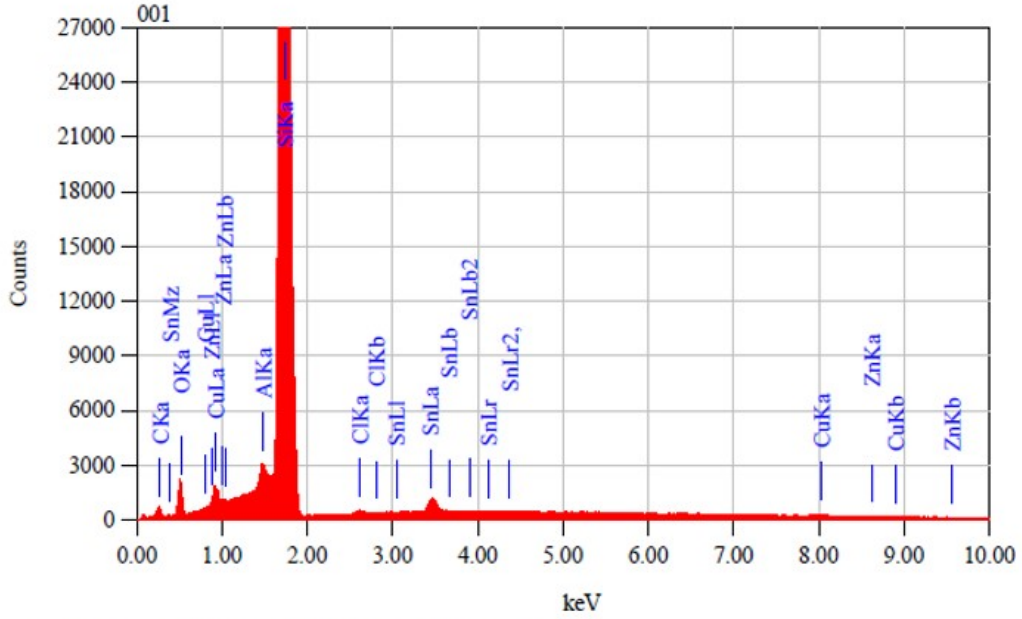


```
Acquisition Parameter
Instrument    : JCM-6000PLUS
Acc. Voltage  : 15.0 kV
Probe Current: 1.00000 nA
PHA mode      : Standard
Real Time     : 200.00 sec
Live Time     : 155.24 sec
Dead Time     : 21 %
Counting Rate: 16838 cps
Energy Range :  0 - 20 keV
```

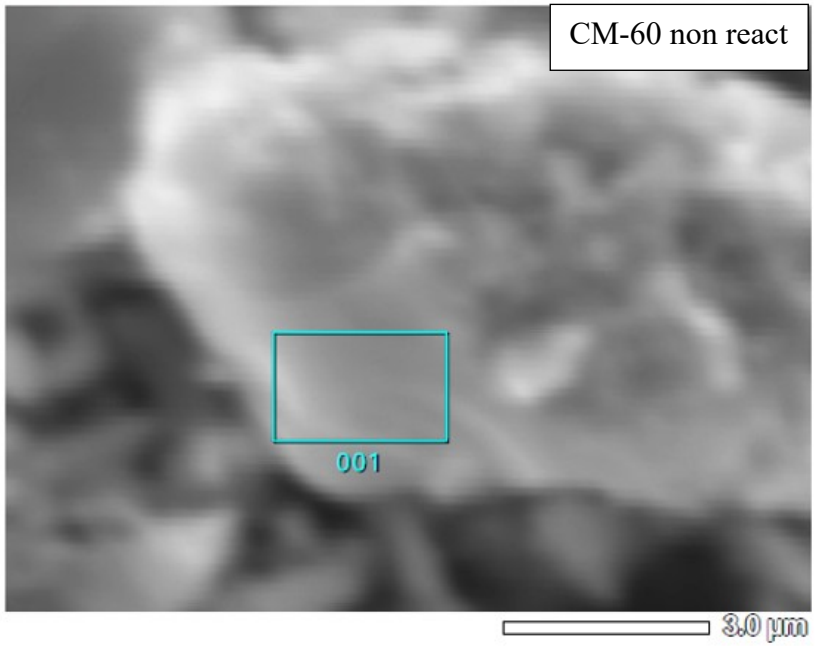

ZAF Method Standardless Quantitative Analysis
Fitting Coefficient : 0.2302

Element	(keV)	Mass%	Sigma	Atom%	Compound	Mass%	Cation	K
C K*	0.277	4.79	0.06	10.45				0.2403
O K*	0.525	3.41	0.04	5.58				1.5187
Al K	1.486	0.46	0.01	0.45				0.4838
Si K*	1.739	88.62	0.10	82.63				95.6348
Cl K*	2.621	0.19	0.01	0.14				0.1433
Cu K*	8.040	0.95	0.05	0.39				0.8583
Zn K*	8.630	0.06	0.04	0.03				0.0572
Sn L*	3.442	1.52	0.03	0.34				1.0635
Total		100.00		100.00				

Figure S5. CM-60 non reacted area.

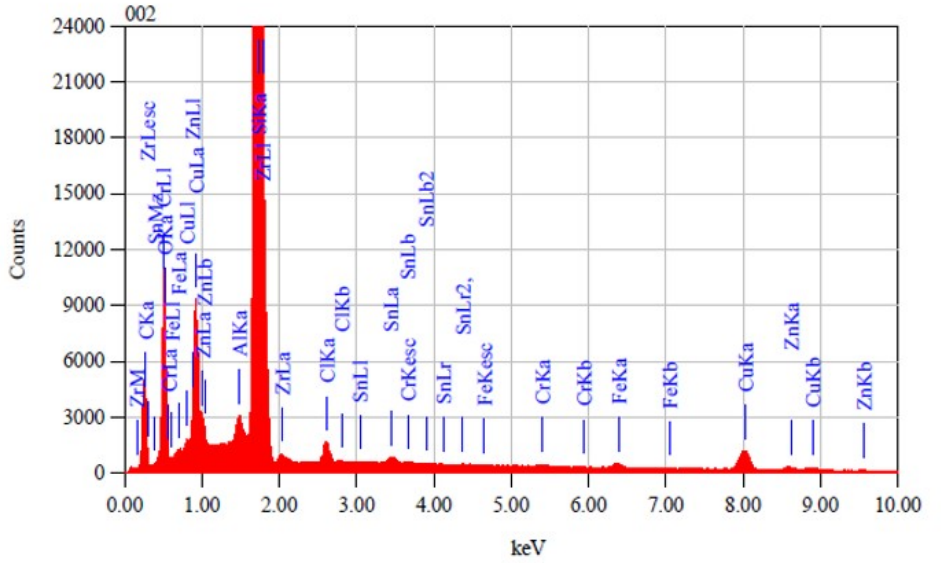

ZAF Method Standardless Quantitative Analysis
Fitting Coefficient : 0.2179

Element	(keV)	Mass%	Sigma	Atom%	Compound	Mass%	Cation	
C K	0.277	20.74	0.09	36.46				2.488
O K	0.525	15.18	0.07	20.03				9.858
Al K	1.486	0.49	0.01	0.38				0.604
Si K	1.739	52.26	0.07	39.29				72.405
Cl K	2.621	0.72	0.01	0.43				0.904
Cr K*	5.411	0.23	0.01	0.09				0.324
Fe K*	6.398	0.72	0.02	0.27				1.007
Cu K	8.040	7.19	0.09	2.39				9.554
Zn K*	8.630	1.31	0.06	0.42				1.734
Zr L	2.042	0.44	0.02	0.10				0.340
Sn L	3.442	0.71	0.02	0.13				0.776
Total		100.00		100.00				

Acquisition Parameter
Instrument : JCM-6000PLUS
Acc. Voltage : 15.0 kV
Probe Current: 1.00000 nA
PHA mode : Standard
Real Time : 200.00 sec
Live Time : 166.37 sec
Dead Time : 15 %
Counting Rate: 11753 cps
Energy Range : 0 - 20 keV

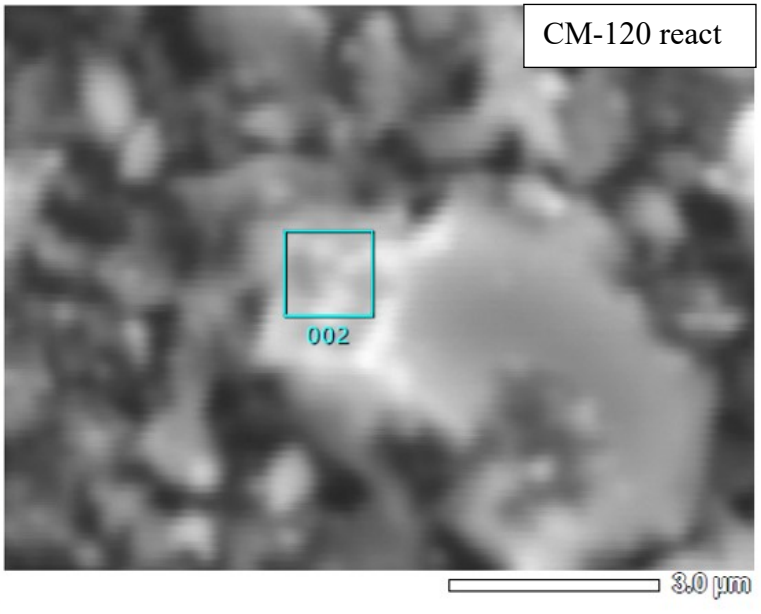

Figure S6. CM-120 reacted area.

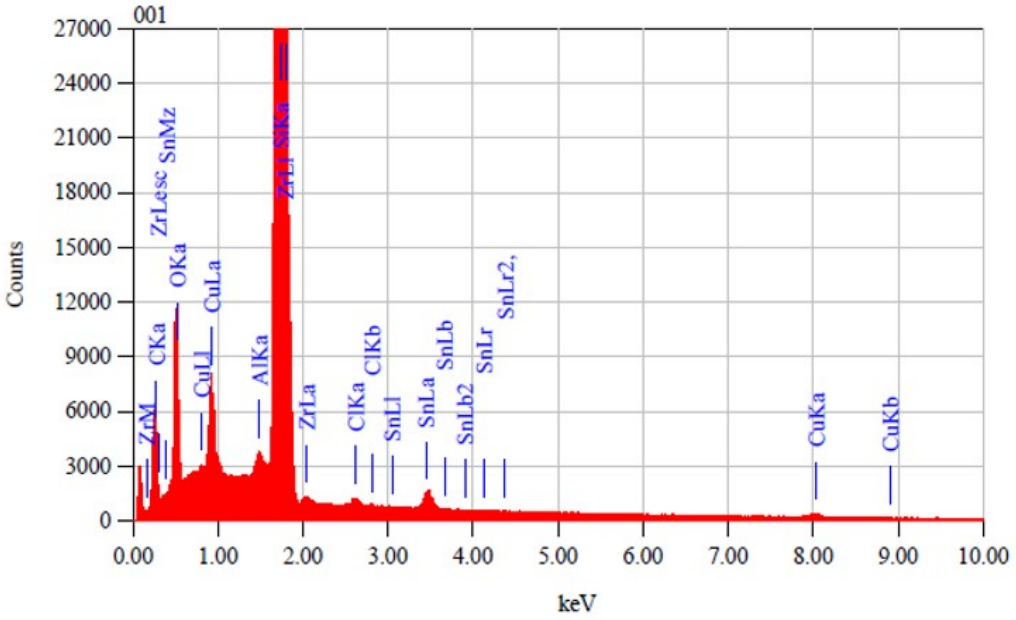


```
Acquisition Parameter
Instrument    : JCM-6000PLUS
Acc. Voltage  : 15.0 kV
Probe Current: 1.00000 nA
PHA mode      : Standard
Real Time     : 200.00 sec
Live Time     : 140.96 sec
Dead Time     : 29 %
Counting Rate: 23870 cps
Energy Range :  0 - 20 keV
```

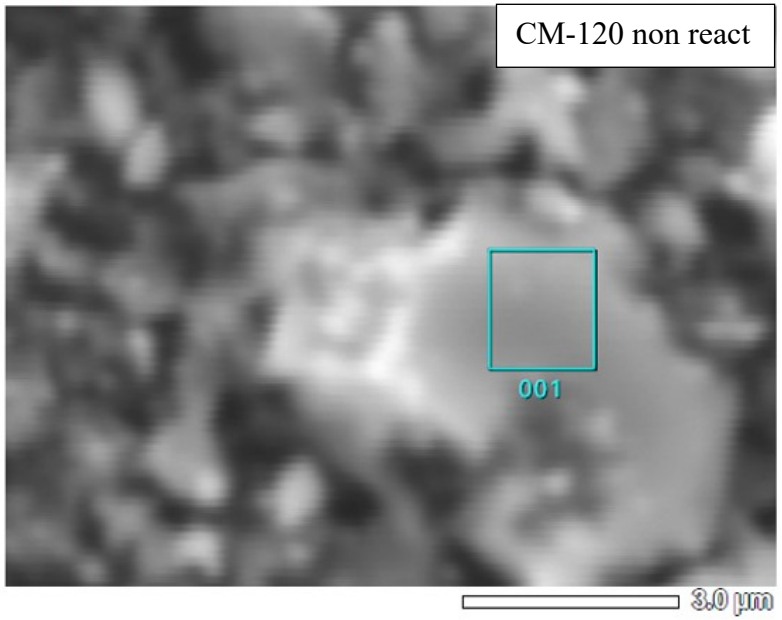

ZAF Method Standardless Quantitative Analysis
Fitting Coefficient : 0.2310

Element	(keV)	Mass%	Sigma	Atom%	Compound	Mass%	Cation	K
C K	0.277	21.82	0.08	37.45				2.0191
O K	0.525	11.60	0.06	14.95				6.2703
Al K	1.486	0.30	0.01	0.23				0.3917
Si K*	1.739	63.52	0.07	46.62				88.4548
Cl K	2.621	0.22	0.01	0.13				0.2463
Cu K	8.040	1.09	0.04	0.35				1.3110
Zr L*	2.042	0.35	0.02	0.08				0.2352
Sn L*	3.442	1.10	0.02	0.19				1.0716
Total		100.00		100.00				

Figure S7. CM-120 non reacted area.

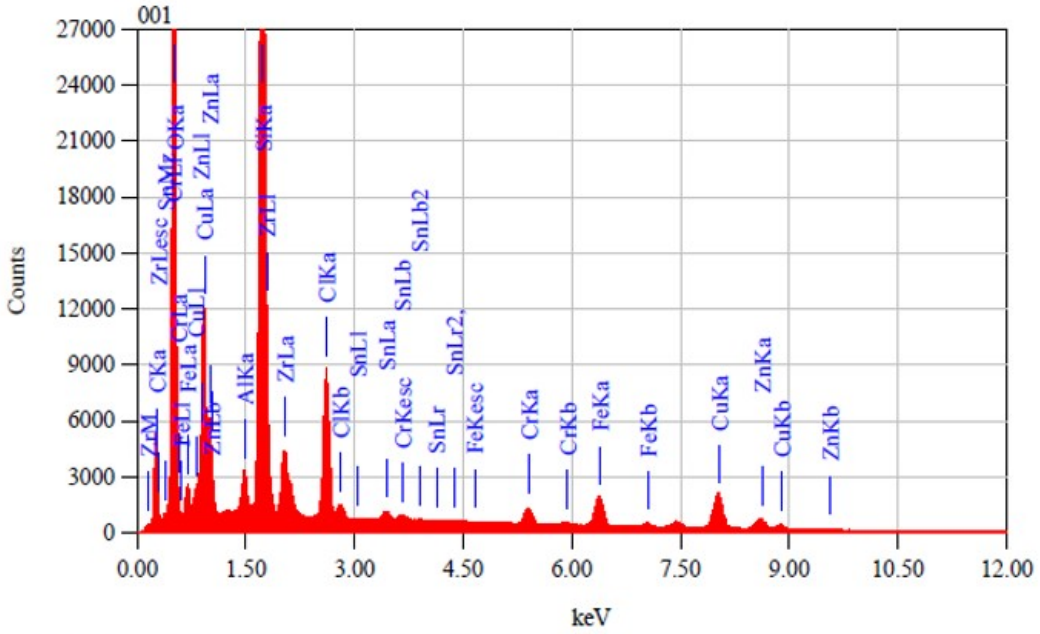


```
Acquisition Parameter
Instrument    : JCM-6000PLUS
Acc. Voltage  : 15.0 kV
Probe Current: 1.00000 nA
PHA mode      : Standard
Real Time     : 200.00 sec
Live Time     : 173.19 sec
Dead Time     : 13 %
Counting Rate: 9884 cps
Energy Range :  0 - 20 keV
```

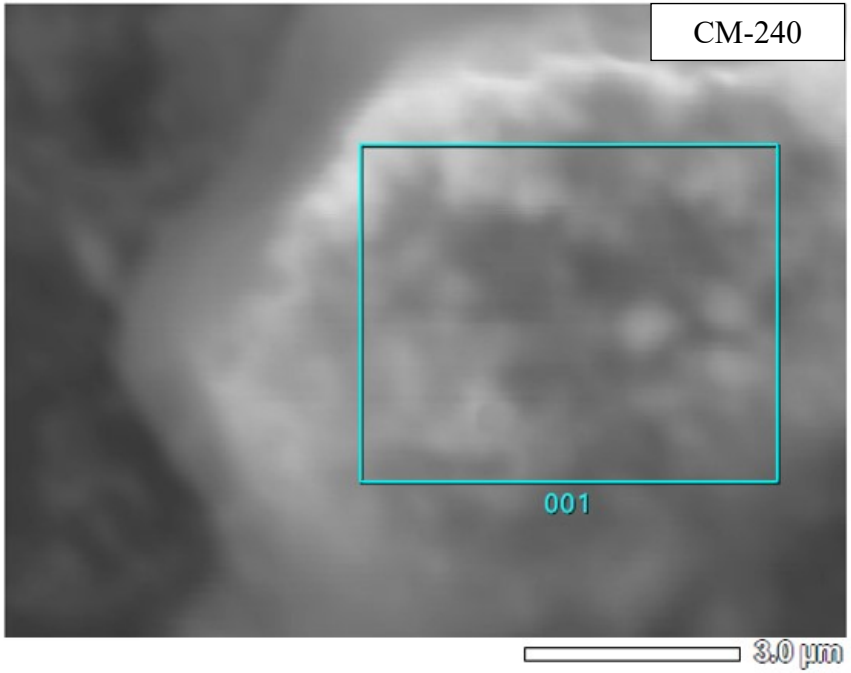

ZAF Method Standardless Quantitative Analysis
Fitting Coefficient : 0.2130

Element	(keV)	Mass%	Sigma	Atom%	Compound	Mass%	Cation	K
C K	0.277	11.42	0.05	21.20				2.1830
O K	0.525	36.10	0.09	50.33				31.6219
Al K	1.486	0.89	0.01	0.74				0.8657
Si K	1.739	19.66	0.05	15.61				23.2036
Cl K	2.621	4.44	0.02	2.79				6.1322
Cr K*	5.411	1.55	0.03	0.67				2.2447
Fe K	6.398	4.38	0.05	1.75				6.4037
Cu K	8.040	11.66	0.11	4.09				15.8877
Zn K	8.630	4.71	0.09	1.61				6.3934
Zr L*	2.042	4.30	0.04	1.05				4.0476
Sn L	3.442	0.89	0.02	0.17				1.0166
Total		100.00		100.00				

Figure S8. CM-240.

3.2. PXRD – data

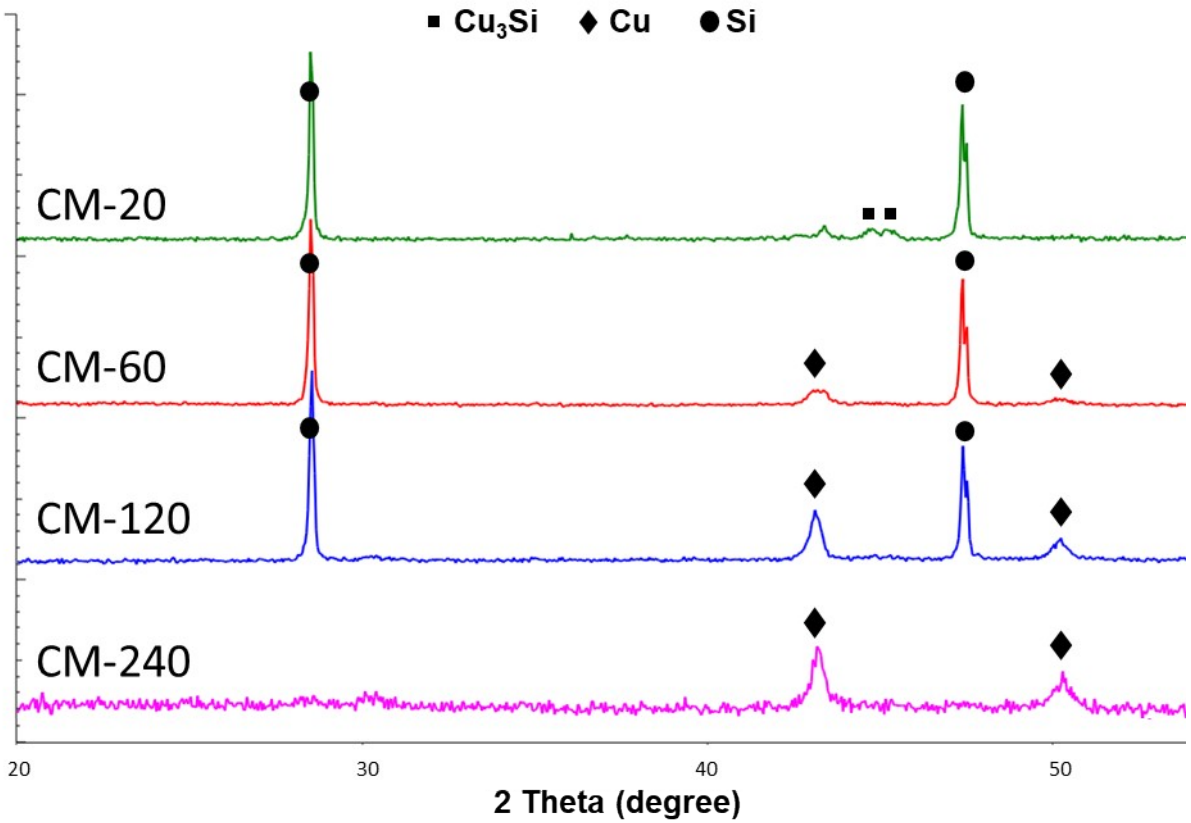

Figure S9. PXRD data of contact mass samples after reaction Si + MeOH (20% CuCl), acceleration 19 g, T = 100 °C, 300 min.

3.3. XPS – spectra, tables and description

Figure S10 shows the Si 2p photoelectron spectra of the studied samples. The surface charge was taken into account by the Si $2p_{3/2}$ peak of Si^0 state with a binding energy of 99.34 eV.[1] When fitting the Si 2p spectra with Gaussian peaks, we took into account the dependence of the chemical shift and peak width on the charge state of silicon atoms.[3–5] For the Si^0 Si $2p_{3/2}$ to Si $2p_{1/2}$ branching ratio was 2:1, and Si $2p_{1/2}$ - Si $2p_{3/2}$ spin-orbit splitting was 0.605 eV. The characteristics of the photoelectron peaks are given in Table S5.

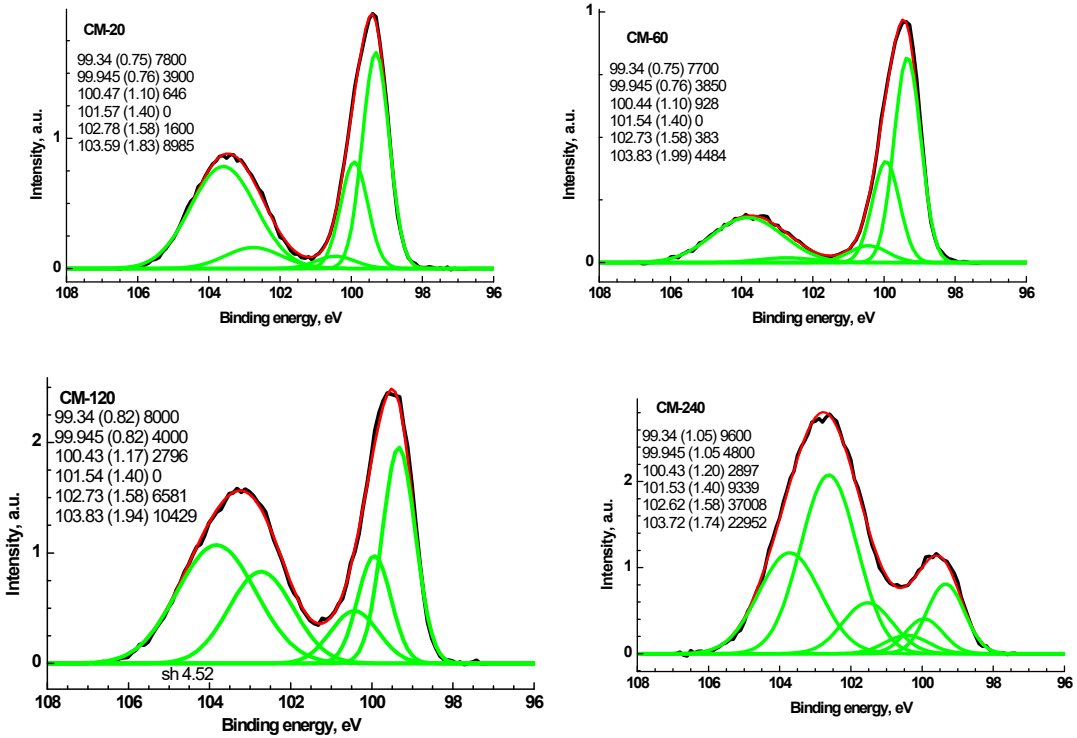

Figure S10. The Si 2p high resolution photoelectron spectra of the contact masses.

Table S5. Parameters of components in the Si 2p photoelectron spectra of the studied samples: E_b – binding energy (eV), W – Gaussian peak width (eV), and I_{rel} – relative intensity.

		Si^0, $2p_{3/2}$	**Si^0, $2p_{1/2}$**	**Si^+**	**Si^{2+}**	**Si^{3+}**	**Si^{4+}**
		I	**II**	**III**	**IV**	**V**	**VI**
CM-20	**E_b**	99.34	99.945	100.47	-	102.78	103.62
	W	0.75	0.76	1.1	-	1.58	1.83
	I_{rel}	0.34	0.17	0.03	-	0.07	0.39
CM-60	**E_b**	99.34	99.945	100.44	-	102.73	103.83
	W	0.75	0.76	1.10	-	1.58	1.99
	I_{rel}	0.44	0.22	0.05	-	0.02	0.26
CM-120	**E_b**	99.34	99.945	100.44	-	102.73	103.83
	W	0.82	0.82	1.17	-	1.58	1.94
	I_{rel}	0.25	0.13	0.09	-	0.21	0.33
CM-240	**E_b**	99.34	99.945	100.43	101.53	102.62	103.72
	W	1.05	1.05	1.20	1.4	1.58	1.74
	I_{rel}	0.11	0.06	0.03	0.11	0.43	0.27

The high resolution C 1s spectra are presented in Figure S11 and their characteristics are presented in Table S6.

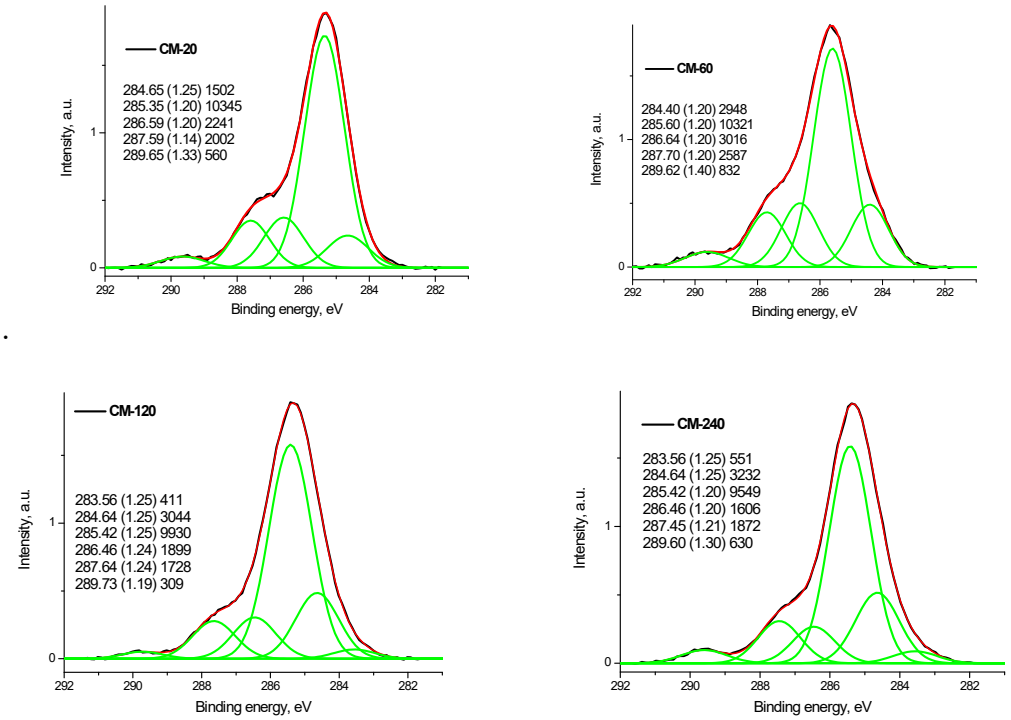

Figure S11. The C 1s photoelectron spectra of the contact masses.

It should be noted that when taking into account the surface charging by the Si^0 state, the binding energies given for the C-C/C-H groups differ markedly from the value of 284.8 eV, most often used for this purpose.[6–8] The most likely reason for this phenomenon may be the manifestation of differential charging. This means that between the C-C/C-H groups and the silicon atoms in the Si^0 state there are areas that prevent the equalization of charges in them formed during the process of photoelectron emission.

In other words, these areas can acquire a charge similar to that formed in areas containing silicon atoms in the Si^0 state or in areas containing C-C/C-H groups. When taking into account corrections of the binding energies of photoelectron peaks based on the C-C/C-H group, slightly different binding energies were obtained, which are given in the row designated $\mathbf{E_b}$ (C) (Table S6). In this case, binding energies lower than 284.8 eV can be attributed to C=C bonds, low molar mass fragments that do not contain C-O bonds, and metal-carbon (M-C) bonds.[6,9]

Table S6. Parameters of components in the C 1s photoelectron spectra of the studied samples: E_b – binding energy (eV), W – Gaussian peak width (eV), and I_{rel} – relative intensity.

Sample	Group	C-C/C-H/M-C	C=C	C-C/C-H	C-O-C	C=O/O-C-O	C(O)O
CM-20	**E_b (Si)**		284.65	285.35	286.59	287.59	289.65
	E_b (C)		284.1	284.8	286.04	287.04	289.1
	W		1.25	1.2	1.2	1.14	1.33
	I_{rel}		0.09	0.62	0.13	0.12	0.03
CM-60	**E_b (Si)**		284.4	285.6	286.6	287.7	289.62
	E_b (C)		283.6	284.8	285.8	286.9	288.82
	W		1.2	1.2	1.2	1.2	1.4
	I_{rel}		0.15	0.52	0.15	0.13	0.04
CM-120	**E_b (Si)**	283.56	284.64	285.42	286.46	287.64	289.73
	E_b (C)	282.94	284.02	284.8	285.84	287.02	289.11
	W	1.25	1.25	1.25	1.24	1.24	1.19
	I_{rel}	0.02	0.18	0.57	0.11	0.1	0.02
CM-240	**E_b (Si)**	283.56	284.64	285.42	286.46	287.45	289.6
	E_b (C)	282.94	284.02	284.8	285.84	286.83	288.98
	W	1.25	1.25	1.2	1.2	1.21	1.3
	I_{rel}	0.03	0.19	0.55	0.09	0.11	0.04

The Sn $3d_{5/2}$ photoelectron spectra are described by three peaks at ~485.6, 487 and 488 eV. More precise values and other characteristics of the spectra are given in Table S7. It should be noted that an analysis of the literature data showed that the binding energies of the Sn $3d_{5/2}$ peak for possible compounds and combinations of interatomic bonds that could be formed in the analyzed samples are in the range of 484.9 – 487.1 eV, while the maximum binding energy, given in Table S7 is 488.29 eV. The most likely reason for this phenomenon may be the above-mentioned manifestation of differential charging.

In other words, these areas can acquire a charge similar to the charge formed either in areas with silicon atoms in the Si^0 state or in areas containing C-C/C-H groups. Taking into account surface charging based on the C-C/C-H group, binding energies (given in the line designated **E_b** (C)) were obtained that were close to the published data and which can be attributed to the Sn^0, Sn^{2+}/Sn^{3+} and Sn^{4+} states.[1,10–19] This means that the regions of the samples containing tin as well as most of the carbon atoms are isolated from the regions containing silicon.

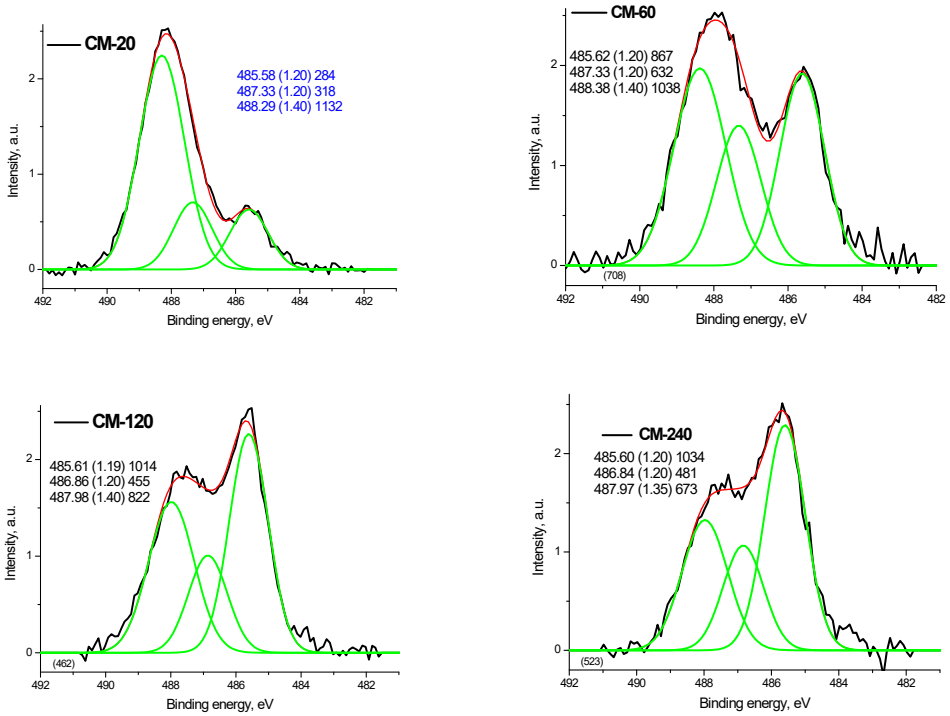

Figure S12. The Sn 3d photoelectron spectra of the contact masses.

Table S7. Parameters of components in the Sn 3d photoelectron spectra of the studied samples: E_b – binding energy (eV), W – Gaussian peak width (eV), and I_{rel} – relative intensity.

		Sn $3d_{5/2}$		
Sample	**State**	**Sn^0**	**Sn^{2+} /Sn^{3+}**	**Sn^{4+}**
CM-20	**E_b** (Si)	485.58	487.33	488.29
	E_b (C)	485.03	486.78	487.74
	W	1.2	1.2	1.4
	I_{rel}	0.16	0.18	0.65
CM-60	**E_b** (Si)	485.62	487.33	488.38
	E_b (C)	484.82	486.53	487.58
	W	1.2	1.2	1.4
	I_{rel}	0.34	0.25	0.41
CM-120	**E_b** (C)	485.61	486.86	487.98
	E_b (C)	484.99	486.24	487.36
	W	1.19	1.2	1.4
	I_{rel}	0.44	0.2	0.36
CM-240	**E_b** (Si)	485.6	486.84	487.97
	E_b (C)	484.98	486.22	487.35
	W	1.2	1.2	1.4
	I_{rel}	0.47	0.22	0.31

In the high-energy region of the Si 2p and C 1s photoelectron spectra of Sn/SiOC composites prepared by the sol–gel method with phenyltriethoxysilane and $SnCl_2 \cdot 2H_2O$ as precursors, the extended “tails” are observed, which indicate the manifestation of differential charging as well.[20]

The Cu 2p photoelectron spectra (Figure S13) are described by two spin-orbit doublets with an interval of about 2.3 eV, the characteristics of which are given in Table S8. The spectra do not contain satellites separated from the main peaks by ~10 – 12 eV, which indicates the absence of the Cu^{2+} state. According to the literature data, the chemical shift for the Cu^+ state in the Cu $2p_{3/2}$ spectra of Cu_2O и CuCl is in the range (+0.1) – (-0.6) eV [8,21–24], which is significantly less than that observed for the samples under study. It should also be noted that the binding energies of the Cu $2p_{3/2}$ peaks given in Table S8 exceed the values characteristic of the Cu^+ and Cu^0 states [1,7,8,11,21–24] by approximately 0.6 eV, the value close to that used for correction the C 1s and Sn 3d spectra.

When using the C-C/C-H group for the charge reference by assigning it a binding energy of 284.8 eV [6–8], the binding energy of the main peaks in the Cu $2p_{3/2}$ spectra of samples CM-20, CM-60, CM-120 and CM-240 are moved to 932.6, 932.4, 932.5, and 932.5 eV, corresponding to the Cu^{+} state. The peaks at higher binding energies should be attributed to the Cu^{0} state. From this we can conclude that the regions of the samples containing copper are surrounded by carbon atoms not associated with oxygen atoms, while silicon atoms are mainly surrounded by either silicon atoms (Si^{0} state) or oxygen atoms (Si^{+}, Si^{2+}, Si^{3+} and Si^{4+} states). This also indicates that the samples under study at least contain two regions that differ in electrical conductivity, which leads to the manifestation of differential charging in the photoelectron spectra.[25–29]

The detection of the Cu^{0} state indicates the presence of particles in which pure copper is surrounded by a non-conducting shell that practically does not interact with copper atoms, but prevents its oxidation. The most probable variant of such a shell can be low-molecular hydrocarbon fragments found in the C 1s spectra.

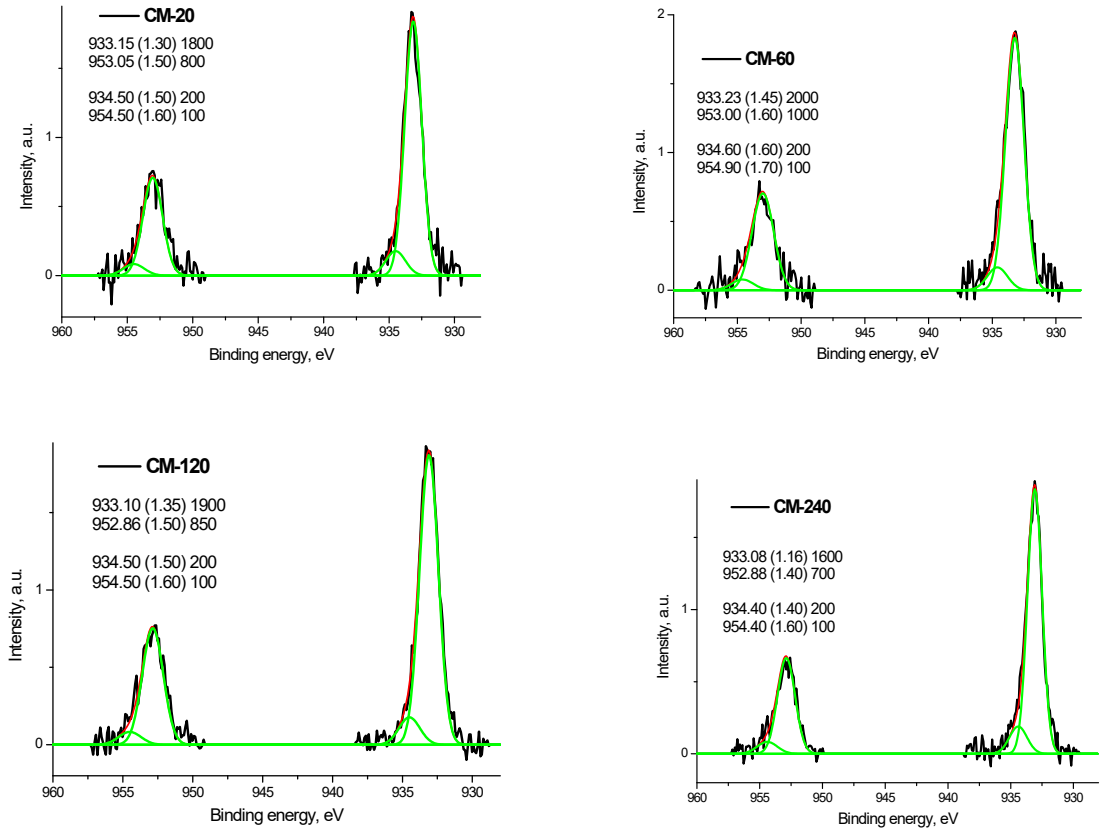

Figure S13. The Cu 2p photoelectron spectra of the contact masses.

Another possible, but unlikely reason for the presence in the Cu 2p spectra of a peak separated from the main peak by ~2.3 eV may be the appearance of the Cu^{3+} state with a characteristic chemical shift of 2.1 eV.[30]

Table S8. Parameters of components in the Cu 2p and Zn 2p photoelectron spectra of the studied samples: E_b – binding energy (eV), W – Gaussian peak width (eV), and I_{rel} – relative intensity.

		Cu				Zn					
		Cu 2p 3/2		Cu 2p 1/2		Zn 2p 3/2			Zn 2p 1/2		
Sample	**State**	**I**	**II**	**I**	**II**	**I**	**II**	**III**	**I**	**II**	**III**
CM-20	**E_b**	933.15	934.50	953.05	954.50	1022.7	1023.87	1025.11	1045.72	1046.98	1048.11
	E_b (C)	932.6	933.95	952.5	953.95	1022.15	1023.32	1024.56	1045.17	1046.43	1047.56
	W	1.3	1.5	1.5	1.6	1.38	1.3	1.3	1.5	1.35	1.5
	I_{rel}	0.60	0.07	0.30	0.03	0.09	0.50	0.07	0.05	0.25	0.03
CM-60	**E_b**	933.23	934.6	953.0	954.9	1022.4	1023.63	1024.9	1045.5	1046.65	1047.0
	E_b (C)	932.43	933.8	952.2	954.1	1021.6	1022.83	1024.1	1044.7	1045.85	1046.2
	W	1.45	1.6	1.6	1.7	1.38	1.38	1.38	1.5	1.5	1.5
	I_{rel}	0.61	0.06	0.30	0.03	0.08	0.49	0.10	0.04	0.24	0.05
CM-120	**E_b**	933.10	934.50	952.86	954.50	1022.2	1023.3	1024.44	1045.2	1046.39	1047.49
	E_b (C)	932.48	933.88	952.24	953.88	1021.58	1022.68	1023.82	1044.58	1045.77	1046.87
	W	1.35	1.5	1.5	1.6	1.38	1.38	1.38	1.5	1.5	1.5
	I_{rel}	0.62	0.07	0.28	0.03	0.08	0.49	0.10	0.04	0.24	0.05
CM-240	**E_b**	933.08	934.4	952.88	954.4	1022.3	1023.46	1024.71	1045.5	1046.54	1047.71
	E_b (C)	932.46	933.78	952.26	953.78	1021.68	1022.84	1024.09	1044.88	1045.92	1047.09
	W	1.16	1.4	1.4	1.6	1.38	1.38	1.38	1.5	1.48	1.5
	I_{rel}	0.62	0.08	0.27	0.04	0.07	0.53	0.07	0.04	0.26	0.03

In contrast to the Cu 2p spectra, the Zn 2p spectra are described by three spin-orbit doublets (Figure S14), the characteristics of which are given in Table S8. According to the literature data, the binding energies of the Zn $2p_{3/2}$ peak and the values of the spin-orbit splitting Zn $2p_{1/2}$ - Zn $2p_{3/2}$ weakly depend on the chemical environment.[1,10,37–45,12,22,31–36]

Therefore, the interpretation of the Zn 2p spectra is similar to that of the Cu 2p spectra, that is, the detection of three states in the spectra is due not to chemical interactions, but to differential charging. However, due to the large number of possible options, at this stage, a reliable determination of the immediate environment of zinc atoms is not possible. One can only assert the presence of a non-conducting shell of C-C/C-H groups.

The manifestation of differential charging was discovered by Hong et al.[36] - for a sample containing, according to X-ray diffraction data, ZnO, Zn_2SiO_4, SiO_2, other salts and carbon activated from sawdust; the maximum binding energies for the Zn $2p_{3/2}$ and Zn $2p_{1/2}$ peaks are given to our knowledge related

to oxides, equal to 1024.7 and 1047.8 eV. In our opinion, such a noticeable difference indicates differential charging caused by the formation of shells with low electrical conductivity around Zn containing species.

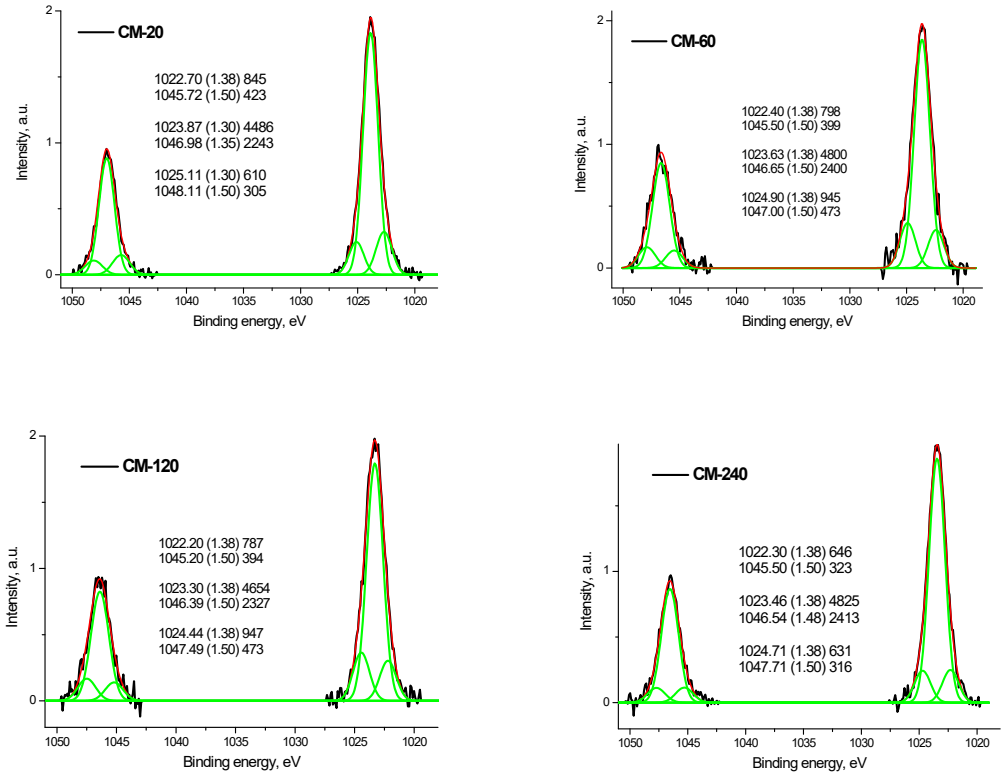

Figure S14. The Zn 2p photoelectron spectra of the contact masses.

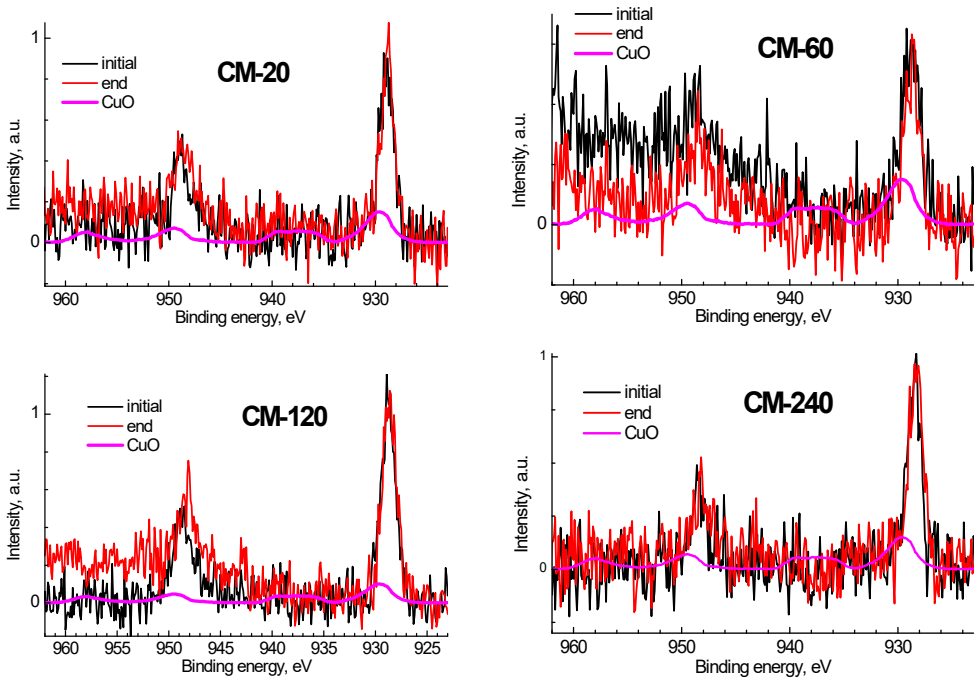

Figure S15. The Cu 2p photoelectron spectra of the contact masses measured at the beginning (curve "initial") and at the end (curve "end") of recording, and the spectrum of CuO (curve "CuO").

Considering the possibility of copper reduction under the X-ray radiation, the Cu 2p spectra were recorded at the beginning and end of the experiment and compared with those of CuO (Figure S15). To reduce the degree of influence, the measurement of spectra began with the Cu 2p spectrum. The presented spectra show the coincidence of the spectral line shapes, taking into account some change in the background, caused mainly by a change in the coefficient of secondary electron emission, and, accordingly, the preservation of the initial state of copper atoms, while the absence of satellites in the range of 938 – 940 eV indicates the absence of Cu^{2+} states.

3.4. NMR

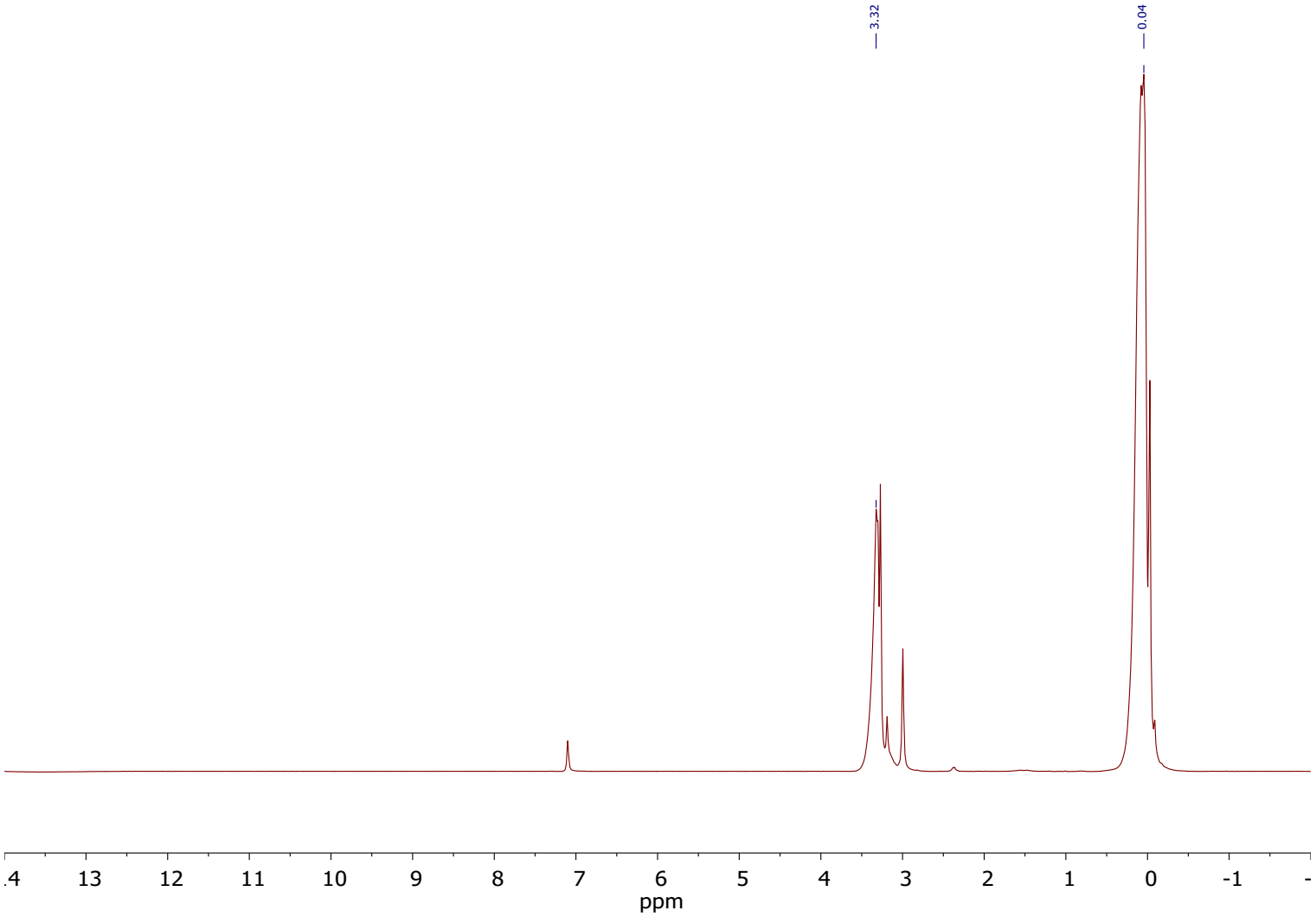

Figure S16. ^{1}H NMR spectrum for liquid products of direct methylmethoxysilanes synthesis.

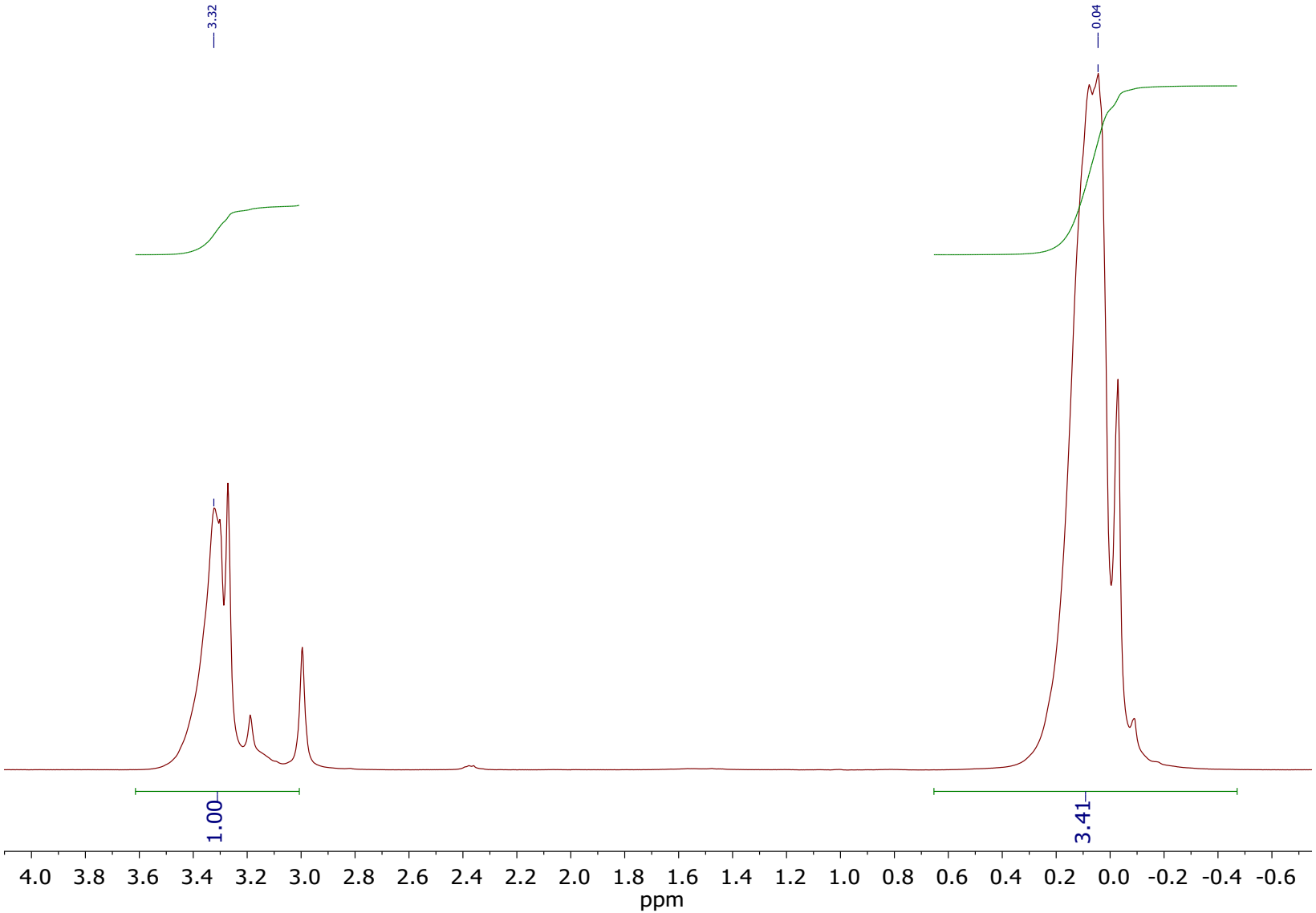

Figure S17. Expanded ^{1}H NMR spectrum for liquid products of direct methylmethoxysilanes synthesis.

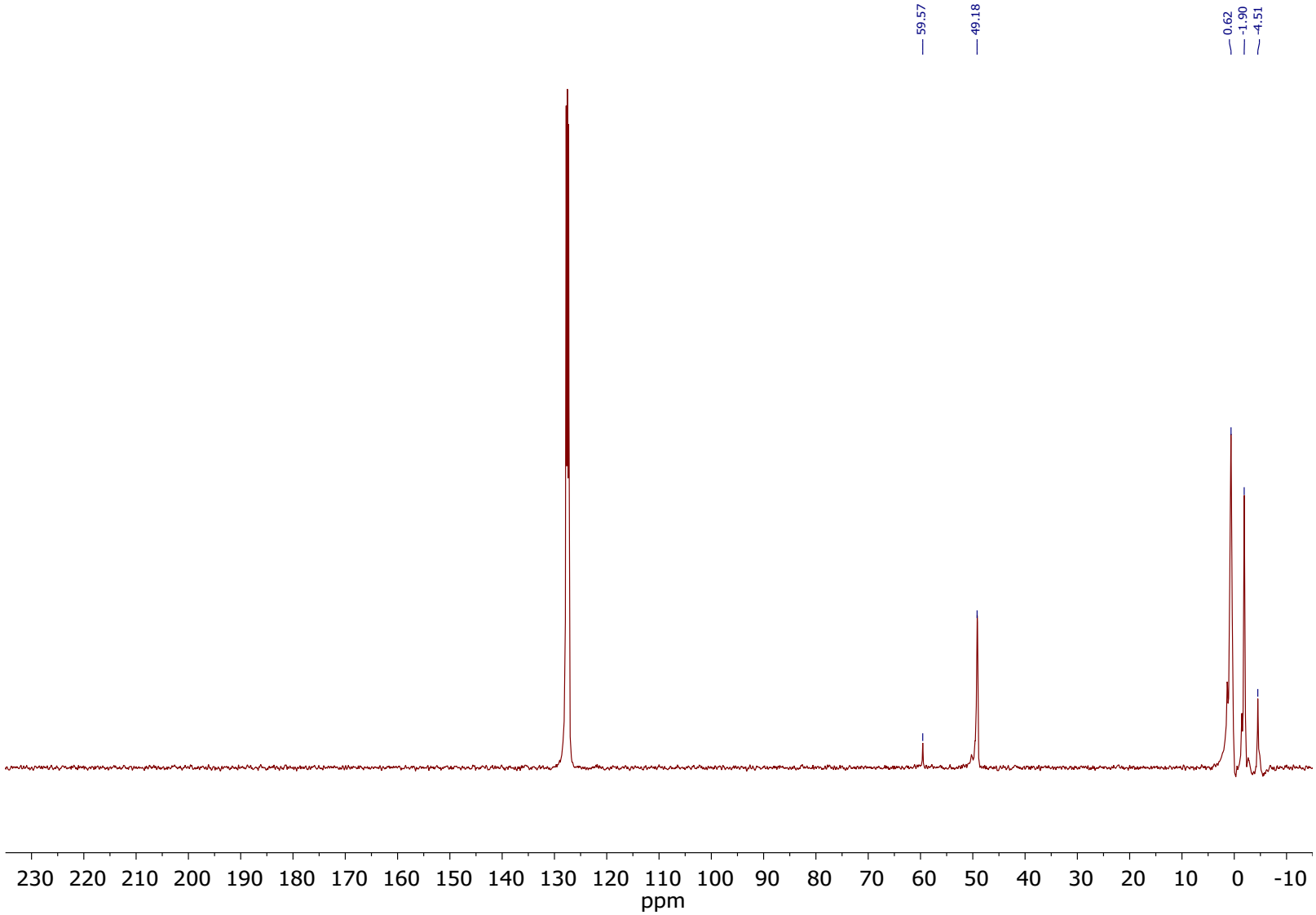

Figure S18. ^{13}C NMR spectrum for liquid products of direct methylmethoxysilanes synthesis.

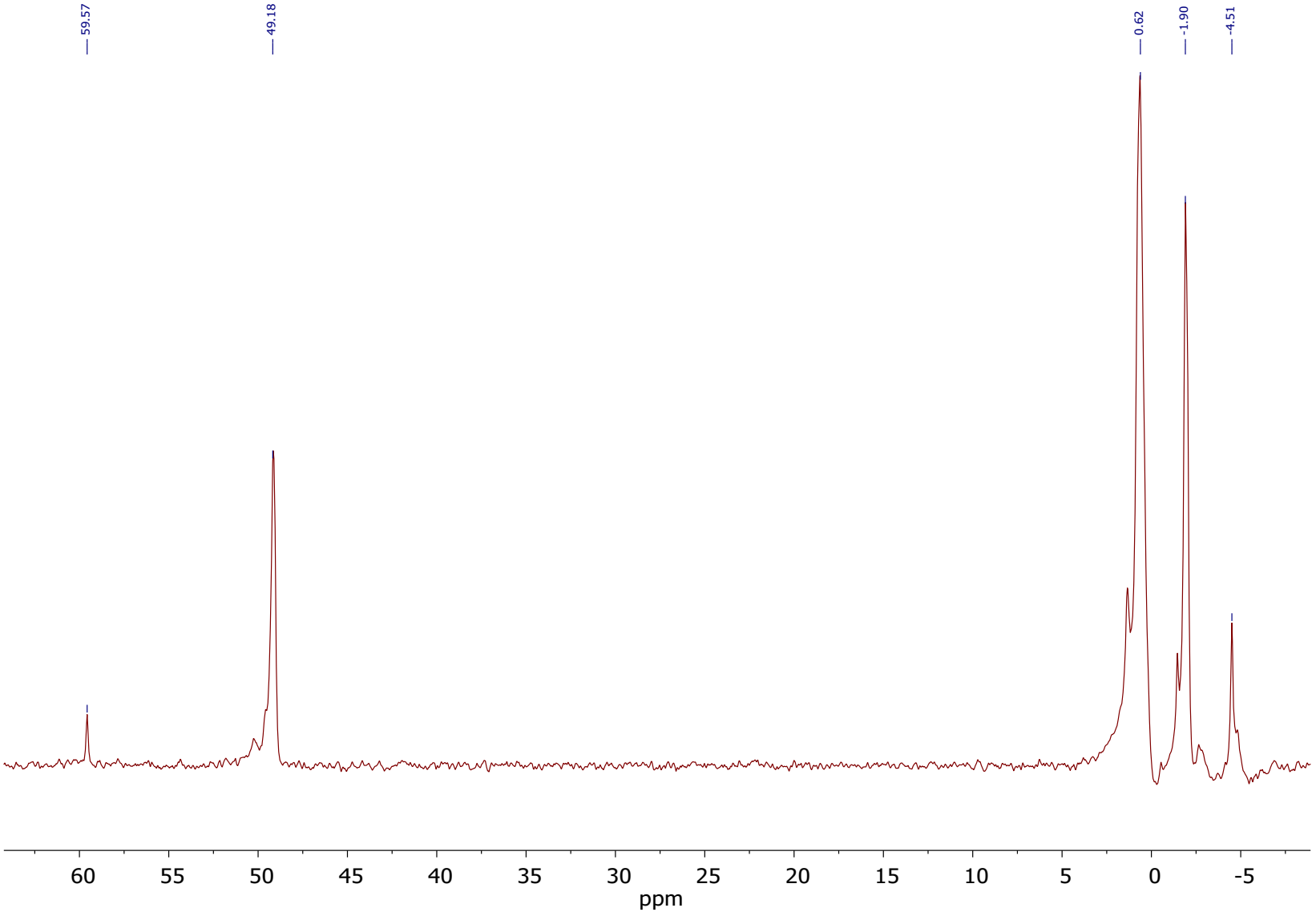

Figure S19. Expanded ^{13}C NMR spectrum for liquid products of direct methylmethoxysilanes synthesis.

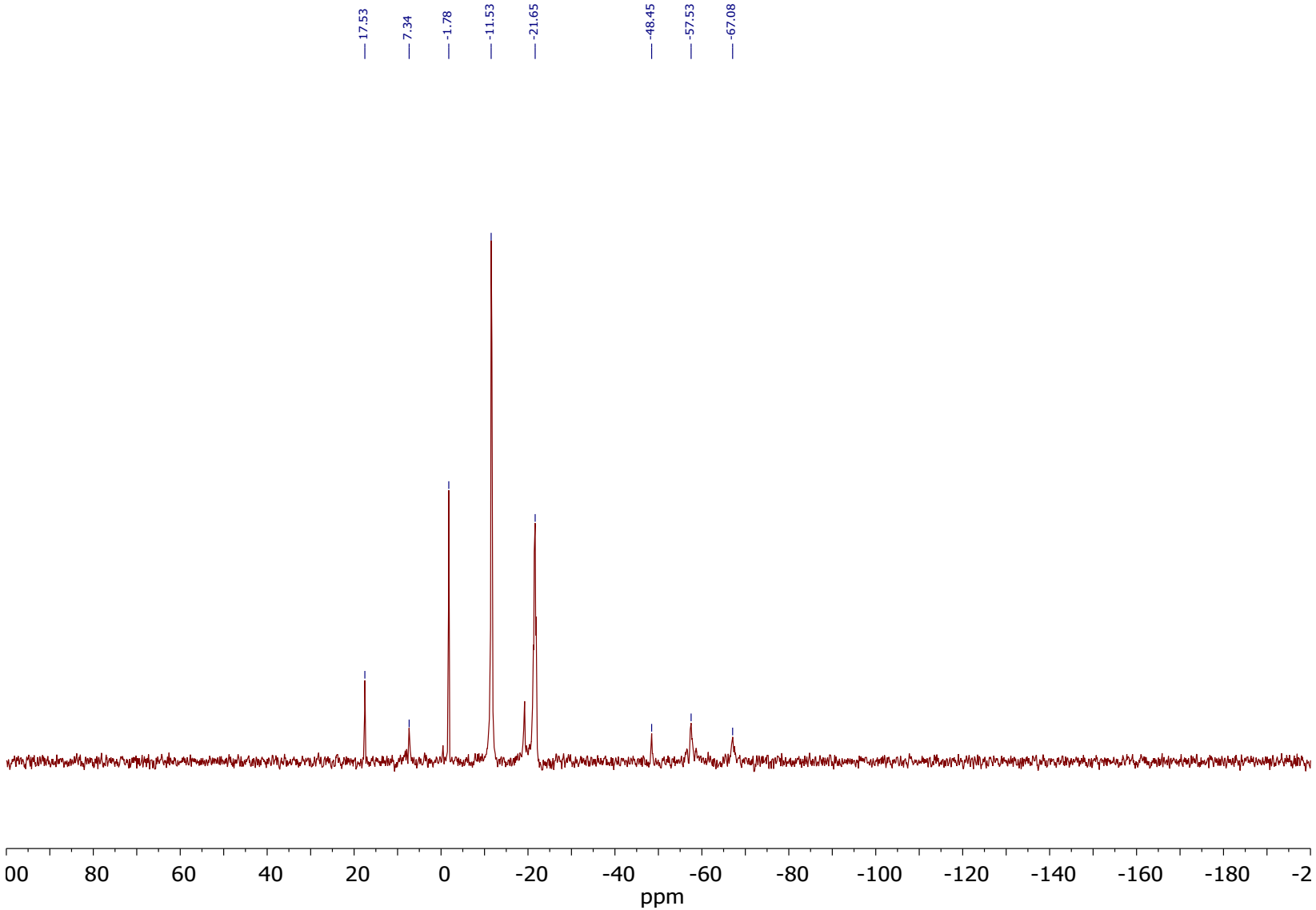

Figure S20. ^{29}Si NMR spectrum for liquid products of direct methylmethoxysilanes synthesis (absence of Q-units).

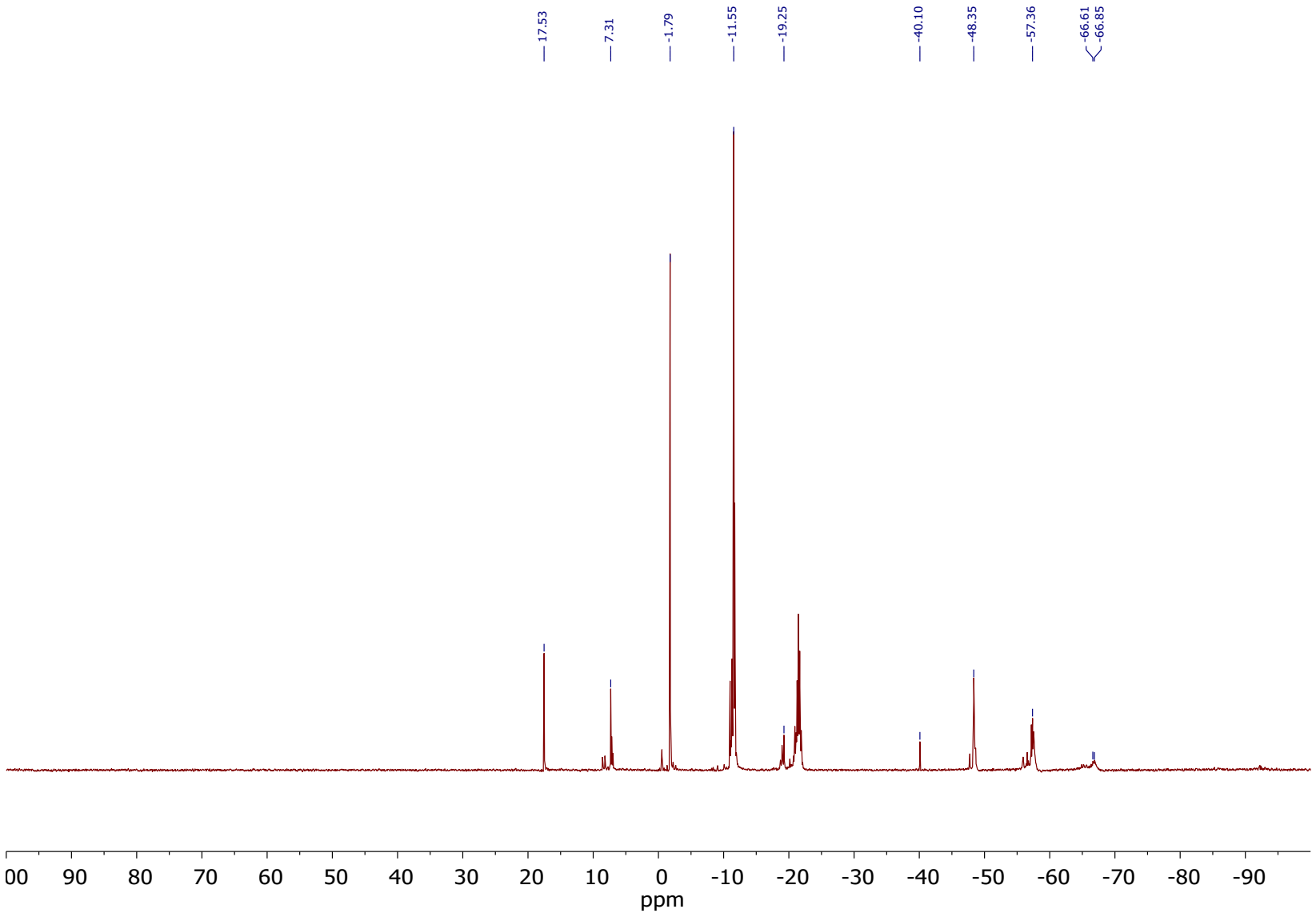

Figure S21. ^{29}Si NMR spectrum for liquid products of direct methylmethoxysilanes synthesis.

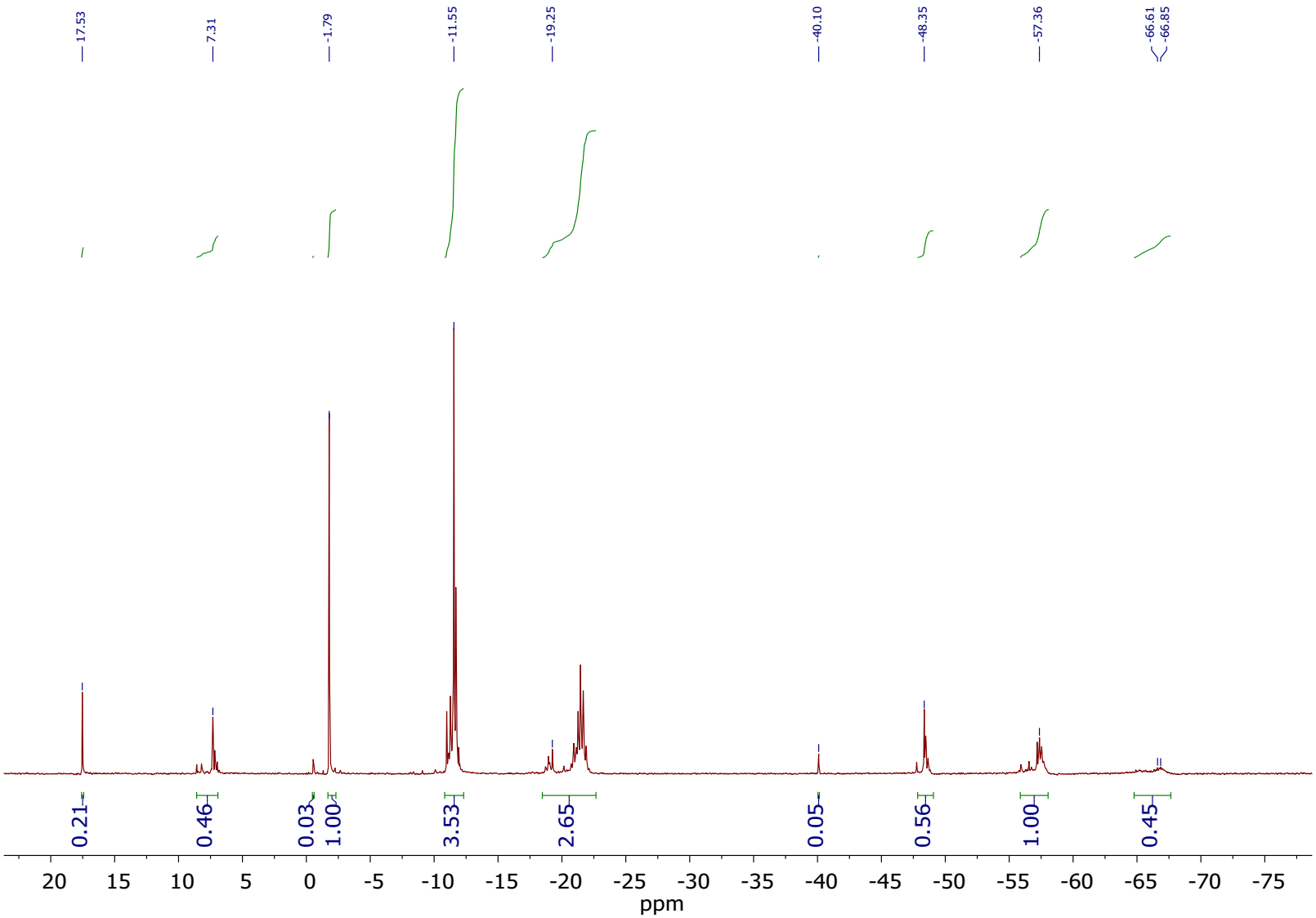

Figure S22. Expanded ^{29}Si NMR spectrum (made with adding of relaxation agent) for liquid products of direct methylmethoxysilanes synthesis.

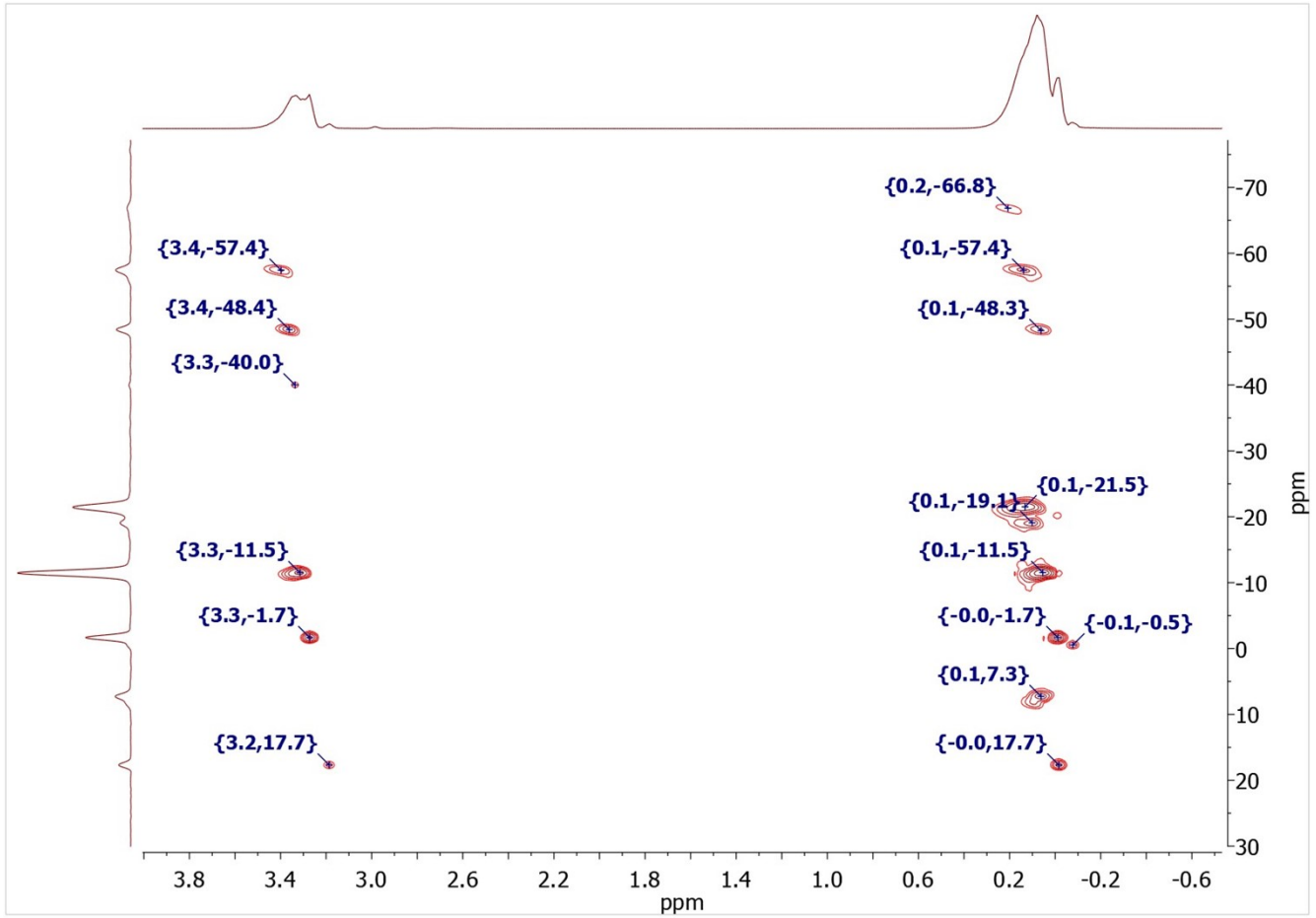

Figure S23. ^{1}H-^{29}Si HMBS NMR spectrum for direct methylmethoxysilanes synthesis.

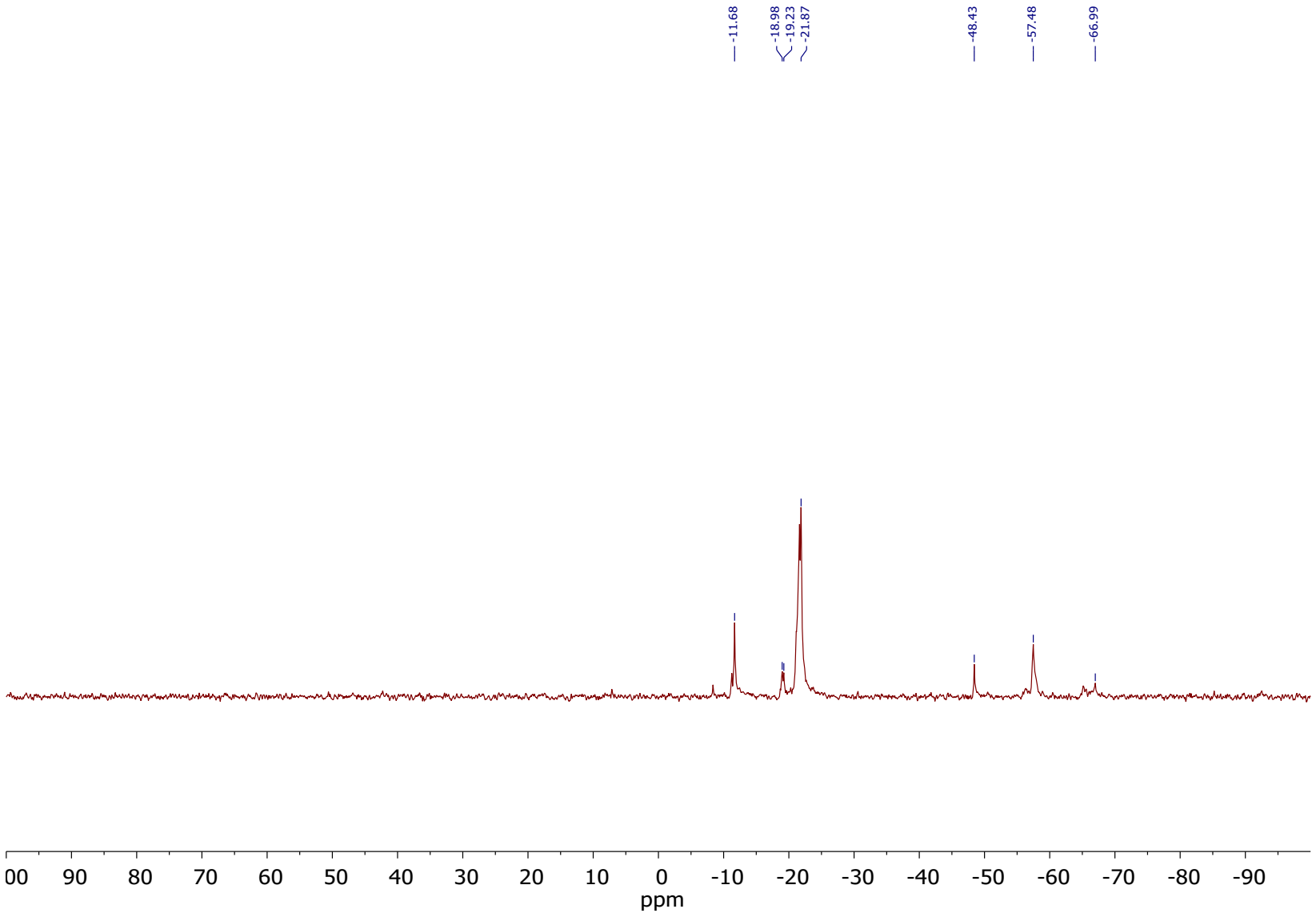

Figure S24. ^{29}Si NMR spectrum for high boiling products of direct methylmethoxysilanes synthesis.

3.5. GC-MS analysis

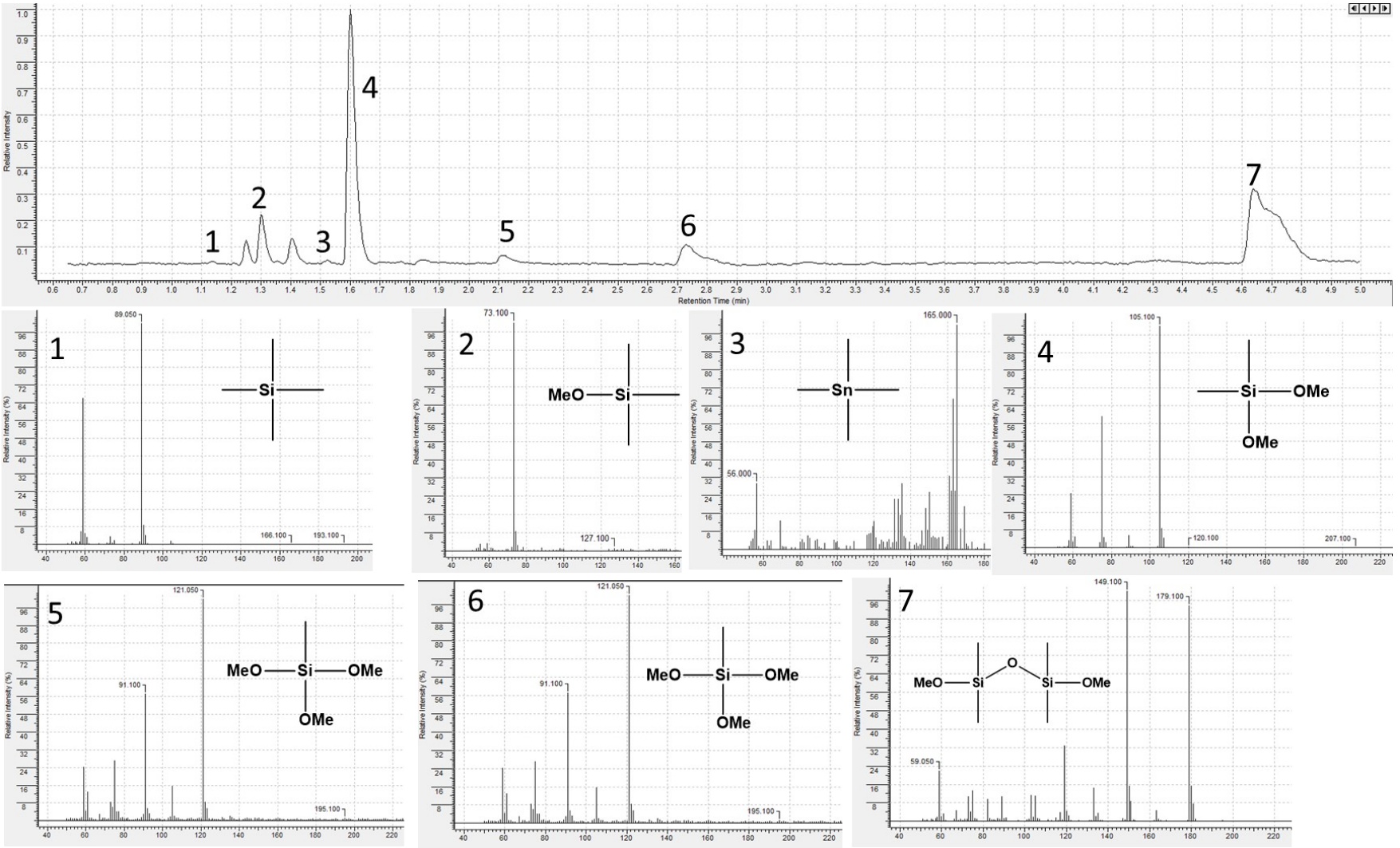

Figure S25. GC-MS analysis of products mixture after the synthesis with dimethyl ether in decane.

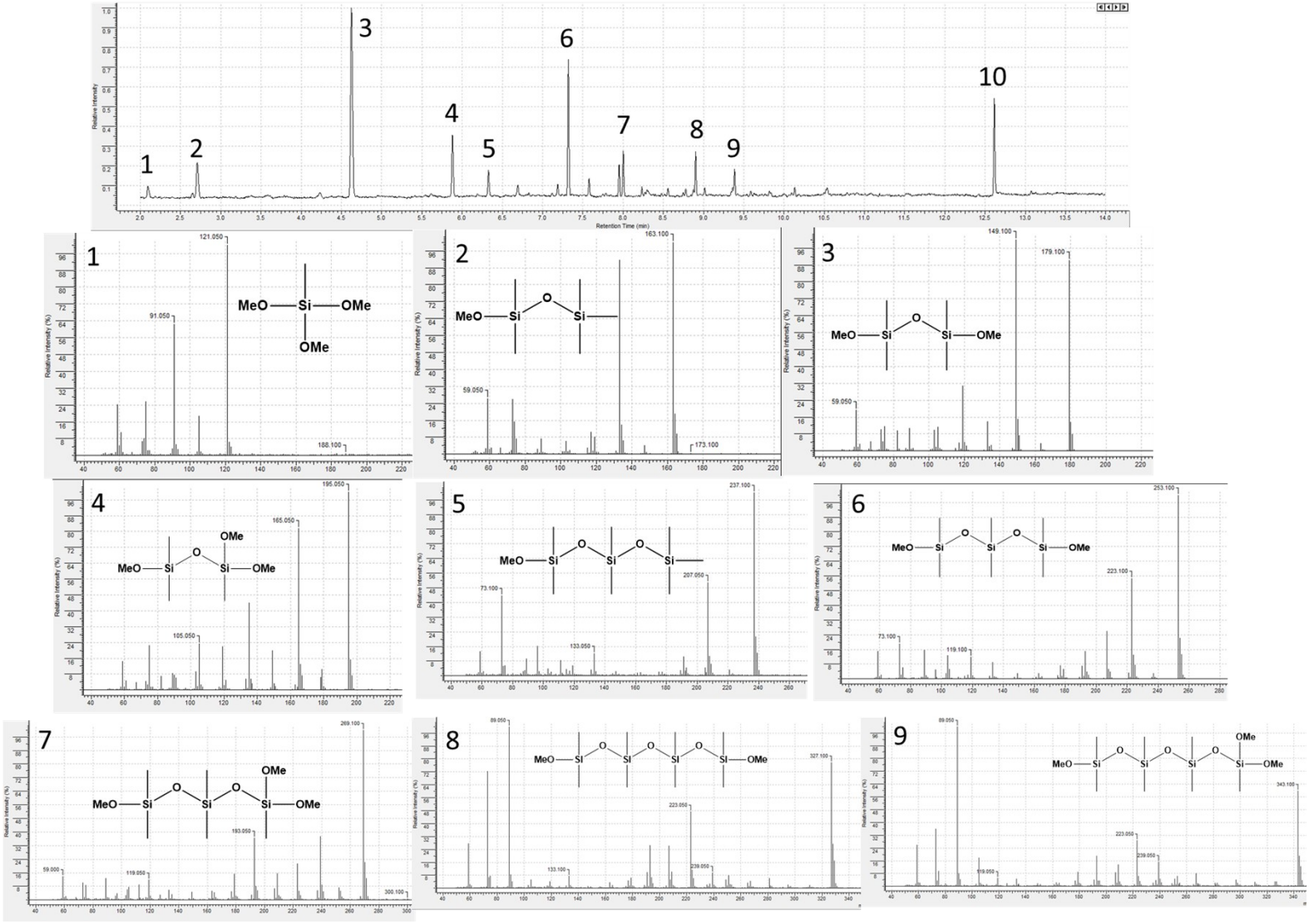

Figure S26. GC-MS analysis of products mixture after the synthesis with dimethyl ether in diethyl ether.

3.6. GC

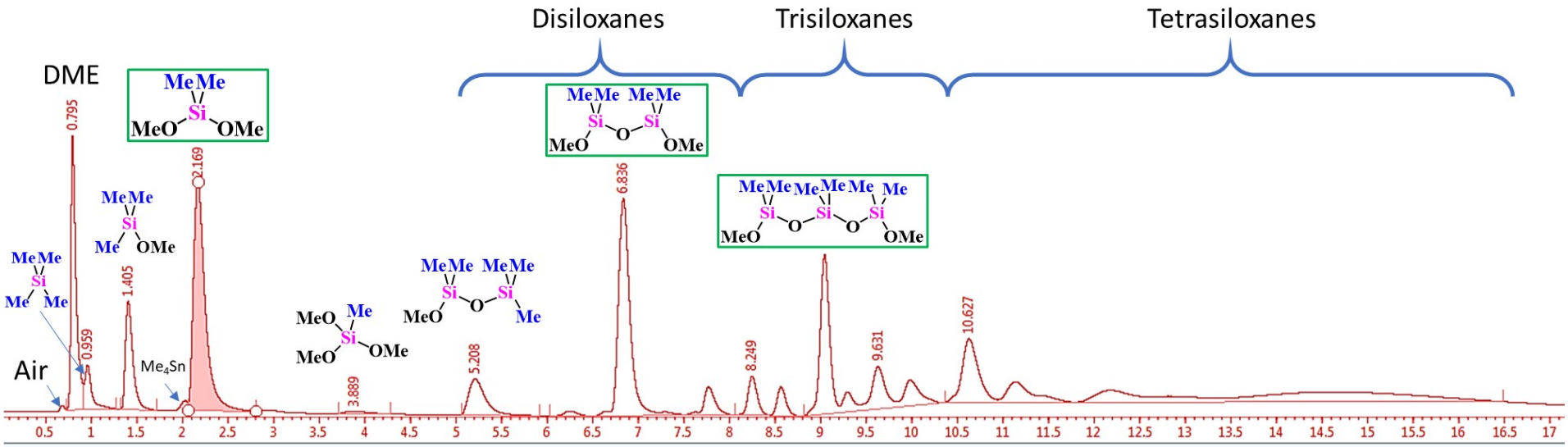

Time, min	Concentration, %	Area
0.795	8.688	1437.122
0.959	1.981	327.728
1.405	5.011	828.768
2.169	16.762	2772.470
3.889	0.311	51.396
5.208	3.719	615.197
6.836	18.264	3021.036
8.249	3.875	640.888
9.631	16.995	2811.083
10.627	24.394	4034.834

Figure S27. GC chromatogram of CM-240 synthesis.

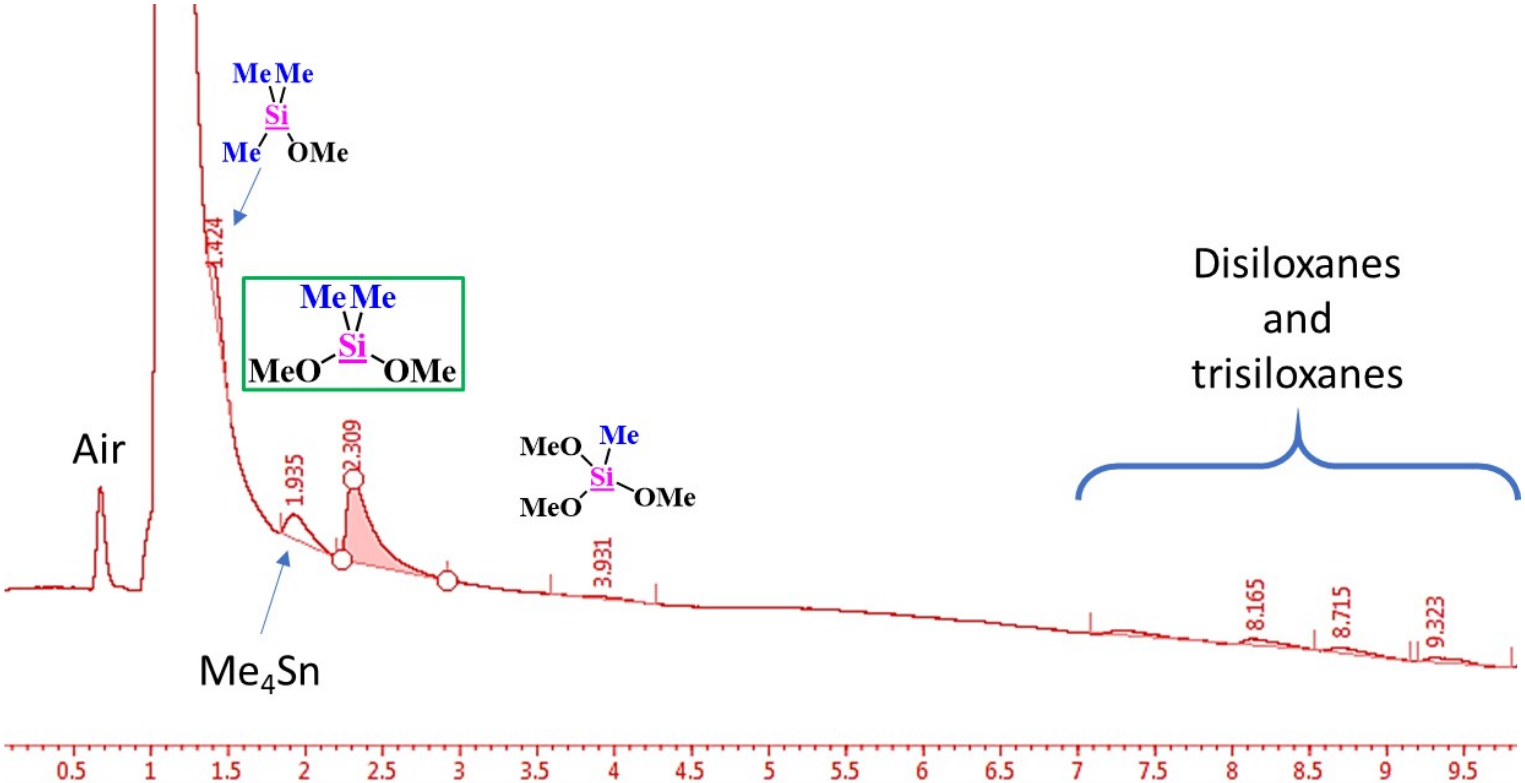

Time, min	Concentration, %	Area
1.424	7.923	17.227
1.935	11.588	25.194
2.309	44.328	96.376
3.931	2.198	4.778
8.165	10.278	22.346
8.715	3.762	8.179
9.323	3.648	7.932

Figure S28. Result of chlorine-free synthesis with Cu as a source of copper (products were characterized with GC-MS).

3.7. GPC

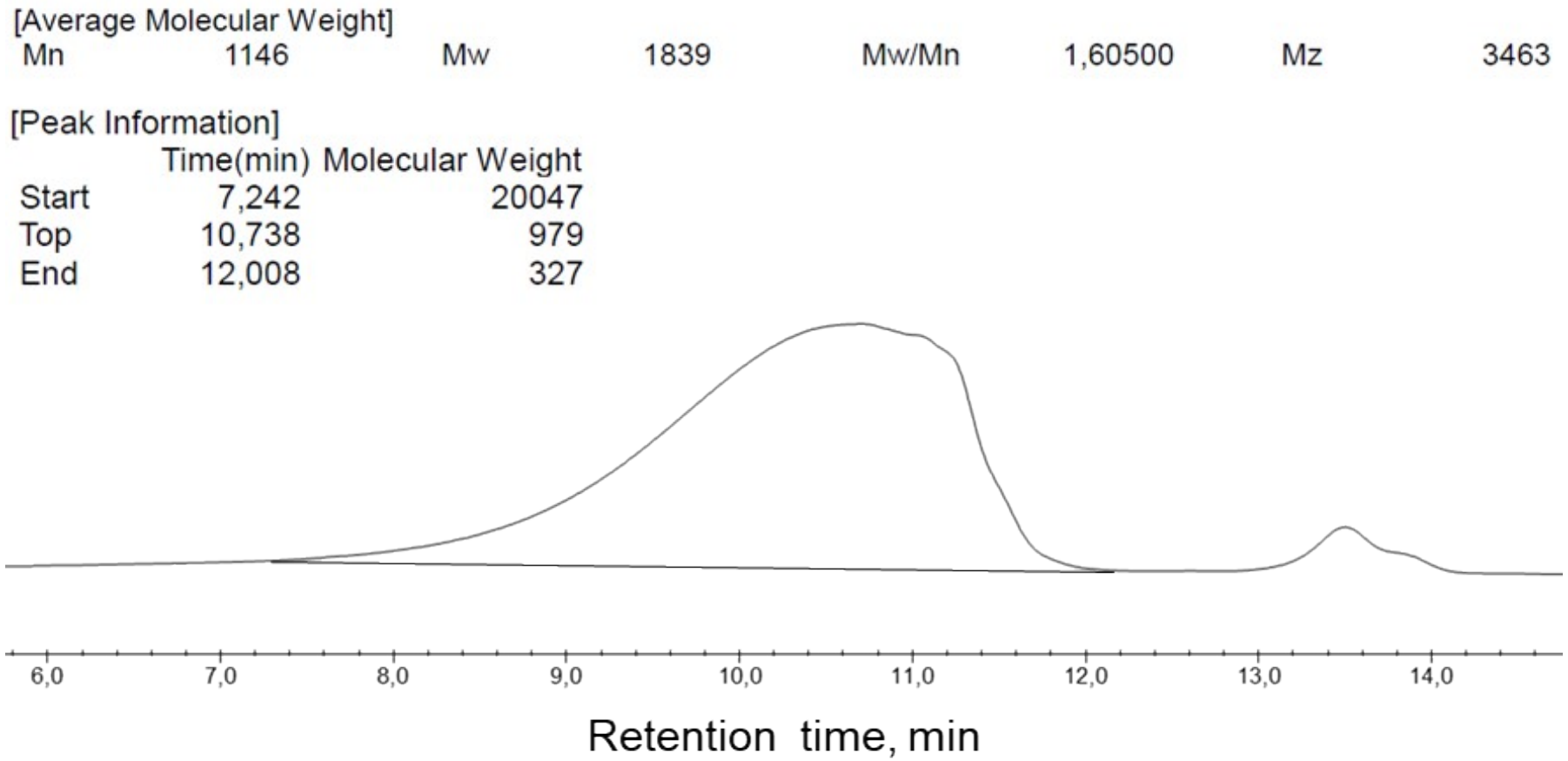

Figure S29. GPC data for high boiling products mixture (toluene, 75 kDa column).

3.8. FTIR

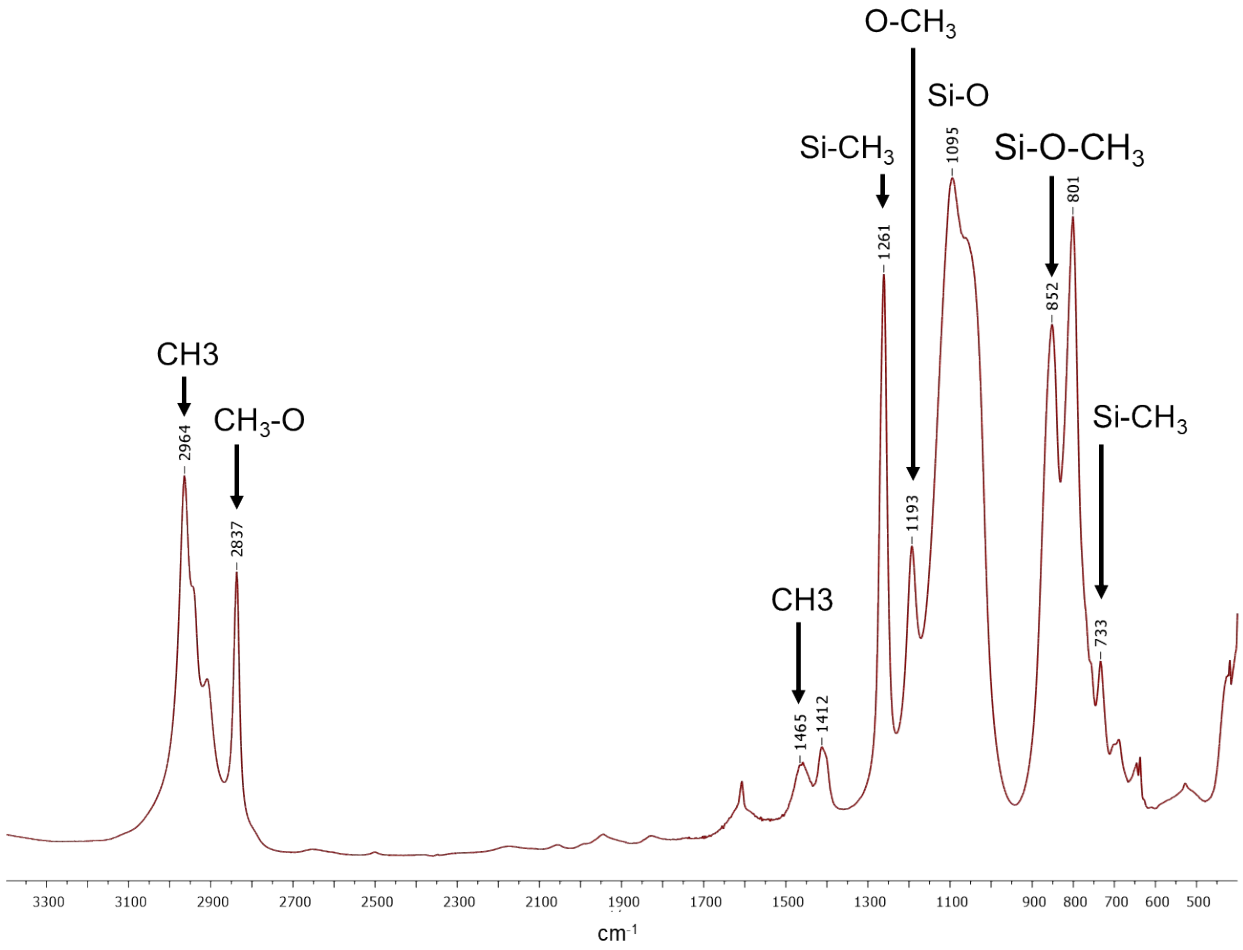

Figure S30. IR spectrum of liquid products mixture.

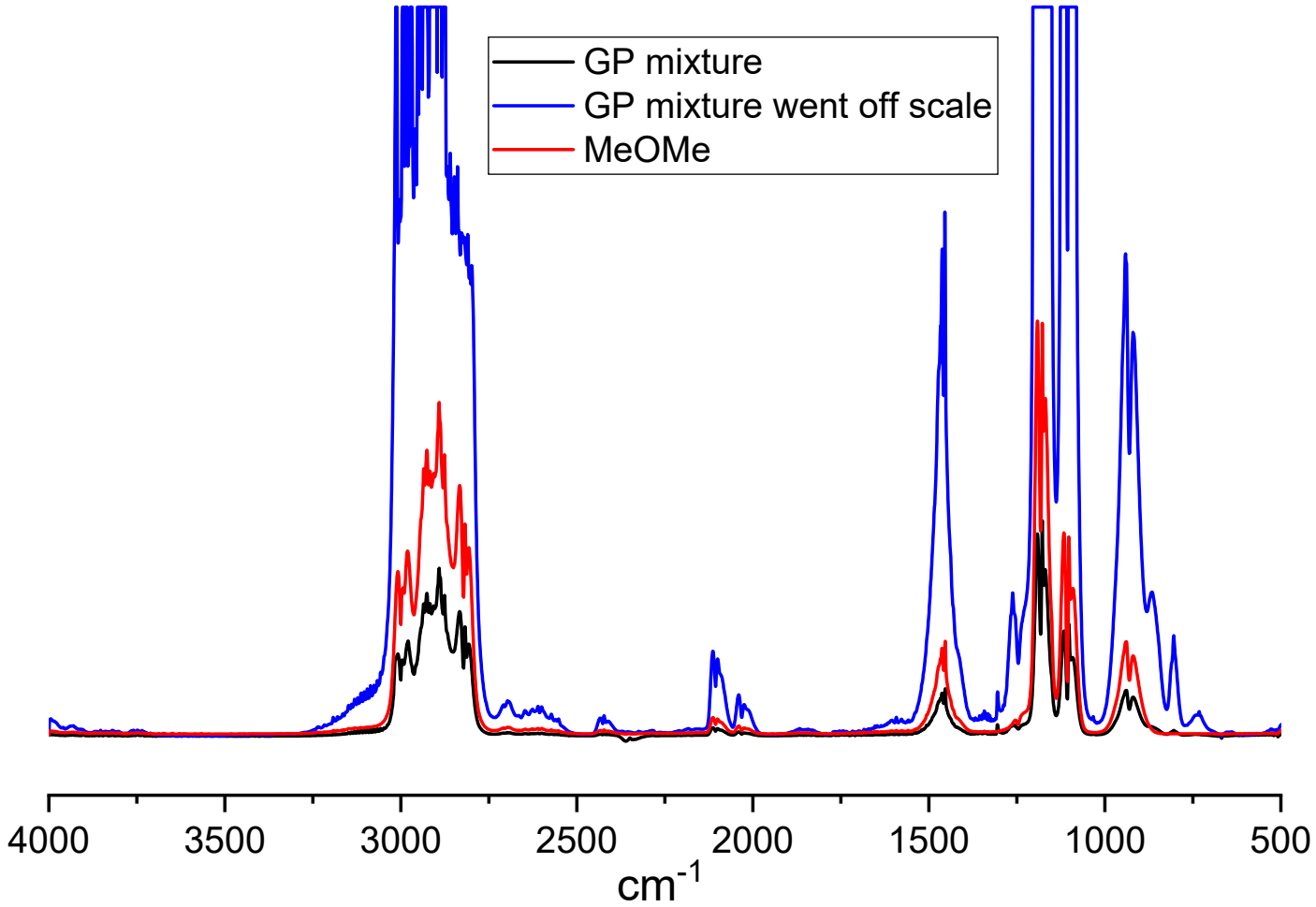

Figure S31. Gas phase FTIR spectroscopy of gaseous products mixture and DME used.

4. References

(1) Powell, C. J. Elemental Binding Energies for X-Ray Photoelectron Spectroscopy. *Appl. Surf. Sci.* **1995**, *89* (2), 141–149. https://doi.org/10.1016/0169-4332(95)00027-5.

(2) Krizhanovskiy, I. N.; Temnikov, M. N.; Anisimov, A. A.; Ratnikov, A. K.; Levin, I. S.; Naumkin, A. V.; Chistovalov, S. M.; Muzafarov, A. M. Direct Synthesis of Tetraalkoxysilanes in a High-Pressure Mechanochemical Reactor. *React. Chem. Eng.* **2022**, *7* (3), 769–780. https://doi.org/10.1039/D1RE00522G.

(3) Himpsel, F. J.; McFeely, F. R.; Taleb-Ibrahimi, A.; Yarmoff, J. A.; Hollinger, G. Microscopic Structure of the SiO2/Si Interface. *Phys. Rev. B* **1988**, *38* (9), 6084–6096. https://doi.org/10.1103/PhysRevB.38.6084.

(4) Oh, J. H.; Yeom, H. W.; Hagimoto, Y.; Ono, K.; Oshima, M.; Hirashita, N.; Nywa, M.; Toriumi, A.; Kakizaki, A. Chemical Structure of the Ultrathin SiO2/Si(100) Interface: An Angle-Resolved Si 2p Photoemission Study. *Phys. Rev. B* **2001**, *63* (20), 205310. https://doi.org/10.1103/PhysRevB.63.205310.

(5) Barbagiovanni, E. G.; Goncharova, L. V.; Simpson, P. J. Electronic Structure Study of Ion-Implanted Si Quantum Dots in a SiO2 Matrix: Analysis of Quantum Confinement Theories. *Phys. Rev. B* **2011**, *83* (3), 035112. https://doi.org/10.1103/PhysRevB.83.035112.

(6) G. Beamson and D. Briggs, High Resolution XPS of Organic Polymers: The Scienta, ESCA300 Database. Chichester; New York: Wiley, 1992.

(7) J. F. Moulder, W. F. Stickle and P. E. Sobol, Handbook of X-Ray Photoelectron Spectroscopy: A Reference Book of Standard Spectra for Identification and Interpretation of XPS Data, 2nd Ed. Perkin-Elmer, Physical Electronics Division, 1995.

(8) A.V. Naumkin, A. Kraut-Vass, S.W. Gaarenstroom, C.J. Powell, and A.Y. Lee. NIST X-Ray Photoelectron Spectroscopy Database (SRD 20), Version 5.0, 2023, Http://Srdata.Nist.Gov/Xps/ (2023-11-23). Https://Dx.Doi.Org/10.18434/T4T88K.

(9) Grüneis, A.; Kummer, K.; Vyalikh, D. V. Dynamics of Graphene Growth on a Metal Surface: A Time-Dependent Photoemission Study. *New J. Phys.* **2009**, *11* (7), 073050. https://doi.org/10.1088/1367-2630/11/7/073050.

(10) Shukla, S.; Seal, S.; Akesson, J.; Oder, R.; Carter, R.; Rahman, Z. Study of Mechanism of Electroless Copper Coating of Fly-Ash Cenosphere

Particles. *Appl. Surf. Sci.* **2001**, *181* (1–2), 35–50. https://doi.org/10.1016/S0169-4332(01)00341-5.

(11) Wang, D.; Miller, A. C.; Notis, M. R. XPS Study of the Oxidation Behavior of the Cu3Sn Intermetallic Compound at Low Temperatures. *Surf. Interface Anal.* **1996**, *24* (2), 127–132. https://doi.org/10.1002/(SICI)1096-9918(199602)24:2<127::AID-SIA110>3.0.CO;2-Z.

(12) Robbiola, L.; Tran, T. T. M.; Dubot, P.; Majerus, O.; Rahmouni, K. Characterisation of Anodic Layers on Cu–10Sn Bronze (RDE) in Aerated NaCl Solution. *Corros. Sci.* **2008**, *50* (8), 2205–2215. https://doi.org/10.1016/j.corsci.2008.06.003.

(13) Li, F.; Song, J.; Yang, H.; Gan, S.; Zhang, Q.; Han, D.; Ivaska, A.; Niu, L. One-Step Synthesis of Graphene / SnO 2 Nanocomposites and Its Application in Electrochemical Supercapacitors. *Nanotechnology* **2009**, *20* (45), 455602. https://doi.org/10.1088/0957-4484/20/45/455602.

(14) Kang, Y.; Park, J.; Kang, Y. Surface Characterization of CuSn Thin Films Deposited by RF Co-sputtering Method. *Surf. Interface Anal.* **2016**, *48* (9), 963–968. https://doi.org/10.1002/sia.5995.

(15) Fondell, M.; Gorgoi, M.; Boman, M.; Lindblad, A. An HAXPES Study of Sn, SnS, SnO and SnO2. *J. Electron Spectros. Relat. Phenomena* **2014**, *195*, 195–199. https://doi.org/10.1016/j.elspec.2014.07.012.

(16) Félix, R.; Llobera-Vila, N.; Hartmann, C.; Klimm, C.; Hartig, M.; Wilks, R. G.; Bär, M. Preparation and In-System Study of SnCl 2 Precursor Layers: Towards Vacuum-Based Synthesis of Pb-Free Perovskites. *RSC Adv.* **2018**, *8* (1), 67–73. https://doi.org/10.1039/C7RA12172E.

(17) Al-Gaashani, R.; Radiman, S.; Tabet, N.; Daud, A. R. Optical Properties of SnO2 Nanostructures Prepared via One-Step Thermal Decomposition of Tin (II) Chloride Dihydrate. *Mater. Sci. Eng. B* **2012**, *177* (6), 462–470. https://doi.org/10.1016/j.mseb.2012.02.006.

(18) Stranick, M. A.; Moskwa, A. SnO2 by XPS. *Surf. Sci. Spectra* **1993**, *2* (1), 50–54. https://doi.org/10.1116/1.1247724.

(19) Stranick, M. A.; Moskwa, A. SnO by XPS. *Surf. Sci. Spectra* **1993**, *2* (1), 45–49. https://doi.org/10.1116/1.1247723.

(20) Xia, K.; Qu, L.; Liu, X.; Han, H.; Hou, Z.; Li, Y.; Deng, S. Effect of SnCl2 Addition on the Structure and Lithium Storage Performance of SiOC Anodes. *Appl. Surf. Sci.* **2020**, *506*, 144775. https://doi.org/10.1016/j.apsusc.2019.144775.

(21) Barreca, D.; Gasparotto, A.; Tondello, E. CVD Cu2O and CuO Nanosystems Characterized by XPS. *Surf. Sci. Spectra* **2007**, *14* (1), 41–51. https://doi.org/10.1116/11.20080701.

(22) Biesinger, M. C.; Lau, L. W. M.; Gerson, A. R.; Smart, R. S. C. Resolving Surface Chemical States in XPS Analysis of First Row Transition Metals, Oxides and Hydroxides: Sc, Ti, V, Cu and Zn. *Appl. Surf. Sci.* **2010**, *257* (3), 887–898. https://doi.org/10.1016/j.apsusc.2010.07.086.

(23) Francisco, M. S. P.; Mastelaro, V. R.; Nascente, P. A. P.; Florentino, A. O. Activity and Characterization by XPS, HR-TEM, Raman Spectroscopy, and BET Surface Area of CuO/CeO 2 -TiO 2 Catalysts. *J. Phys. Chem. B* **2001**, *105* (43), 10515–10522. https://doi.org/10.1021/jp0109675.

(24) Vasquez, R. P. Cu2O by XPS. *Surf. Sci. Spectra* **1998**, *5* (4), 257–261. https://doi.org/10.1116/1.1247881.

(25) Naumkin, A. V.; Vasil'kov, A. Y. Au-Ni and Au-Fe Heterometallic Systems: An X-Ray Photoelectron Spectroscopy Study. *Russ. Chem. Bull.* **2013**, *62* (12), 2559–2566. https://doi.org/10.1007/s11172-013-0373-x.

(26) Vasil'kov, A. Y.; Naumkin, A. V.; Volkov, I. O.; Podshibikhin, V. L.; Lisichkin, G. V.; Khokhlov, A. R. XPS/TEM Characterisation of Pt□Au/C Cathode Electrocatalysts Prepared by Metal Vapour Synthesis. *Surf. Interface Anal.* **2010**, *42* (6–7), 559–563. https://doi.org/10.1002/sia.3269.

(27) Vasil'kov, A.; Batsalova, T.; Dzhambazov, B.; Naumkin, A. XPS Study of Silver and Copper Nanoparticles Demonstrated Selective Anticancer, Proapoptotic, and Antibacterial Properties. *Surf. Interface Anal.* **2022**, *54* (3), 189–202. https://doi.org/10.1002/sia.7038.

(28) Biesinger, M. C. Accessing the Robustness of Adventitious Carbon for Charge Referencing (Correction) Purposes in XPS Analysis: Insights from a Multi-User Facility Data Review. *Appl. Surf. Sci.* **2022**, *597*, 153681. https://doi.org/10.1016/j.apsusc.2022.153681.

(29) Gorham, J. M.; Osborn, W. A.; Woodcock, J. W.; Scott, K. C. K.; Heddleston, J. M.; Hight Walker, A. R.; Gilman, J. W. Detecting Carbon in Carbon: Exploiting Differential Charging to Obtain Information on the Chemical Identity and Spatial Location of Carbon Nanotube Aggregates in Composites by Imaging X-Ray Photoelectron Spectroscopy. *Carbon N. Y.* **2016**, *96*, 1208–1216. https://doi.org/10.1016/j.carbon.2015.10.073.

(30) Steiner, P.; Kinsinger, V.; Sander, I.; Siegwart, B.; Hufner, S.; Politis, C.; Hoppe, R.; Muller, H. P. The Cu Valence in the HighT c Superconductors and in Monovalent, Divalent and Trivalent Copper Oxides Determined from XPS Core Level Spectroscopy. *Zeitschrift fur Anorg. und Allg. Chemier Phys. B Condens. Matter* **1987**, *67* (4), 497–502. https://doi.org/10.1007/BF01304119.

(31) Abdel-wahab, M. S.; Jilani, A.; Alshahrie, A.; Hammad, A. H. Impact of Titanium Ions in the Hexagonal Nanostructured ZnO Thin Films. *J. Mater. Sci. Mater. Electron.* **2018**, *29* (4), 3056–3065. https://doi.org/10.1007/s10854-017-8237-z.

(32) Al-Gaashani, R.; Radiman, S.; Daud, A. R.; Tabet, N.; Al-Douri, Y. XPS and Optical Studies of Different Morphologies of ZnO Nanostructures Prepared by Microwave Methods. *Ceram. Int.* **2013**, *39* (3), 2283–2292. https://doi.org/10.1016/j.ceramint.2012.08.075.

(33) Barreca, D.; Gasparotto, A.; Maccato, C.; Maragno, C.; Tondello, E. ZnO Nanoplatelets Obtained by Chemical Vapor Deposition, Studied by XPS. *Surf. Sci. Spectra* **2007**, *14* (1), 19–26. https://doi.org/10.1116/11.20071001.

(34) Bekermann, D.; Gasparotto, A.; Barreca, D.; Devi, A.; Fischer, R. A. P-Co3O4/n-ZnO, Obtained by PECVD, Analyzed by X-Ray Photoelectron Spectroscopy. *Surf. Sci. Spectra* **2011**, *18* (1), 36–45. https://doi.org/10.1116/11.20111003.

(35) Hameurlaine, E.; Guezzoul, M.; Bouslama, M.; Ouerdane, A.; Derri, A.; Bedrouni, M.; Bensassi, K. B.; Baizid, A.; Abdelkrim, M.; Kharoubi, B. Impact of Indium Doping on ZnO Thin Film Subjected to Appropriate UHV Treatment Characterized by XPS, XRD, and PL Techniques. *Surf. Rev. Lett.* **2022**, *29* (05). https://doi.org/10.1142/S0218625X22500706.

(36) Hong, D.; Zhou, J.; Hu, C.; Zhou, Q.; Mao, J.; Qin, Q. Mercury Removal Mechanism of AC Prepared by One-Step Activation with ZnCl2. *Fuel* **2019**, *235*, 326–335. https://doi.org/10.1016/j.fuel.2018.07.103.

(37) Kaneva, N.; Stambolova, I.; Blaskov, V.; Dimitriev, Y.; Vassilev, S.; Dushkin, C. Photocatalytic Activity of Nanostructured ZnO Films Prepared by Two Different Methods for the Photoinitiated Decolorization of Malachite Green. *J. Alloys Compd.* **2010**, *500* (2), 252–258. https://doi.org/10.1016/j.jallcom.2010.04.020.

(38) Le, T. K.; Nguyen, T. M. T.; Nguyen, H. T. P.; Nguyen, T. K. L.; Lund, T.; Nguyen, H. K. H.; Huynh, T. K. X. Enhanced Photocatalytic Activity of ZnO Nanoparticles by Surface Modification with KF Using Thermal Shock Method. *Arab. J. Chem.* **2020**, *13* (1), 1032–1039. https://doi.org/10.1016/j.arabjc.2017.09.006.

(39) Peng, W. Q.; Cong, G. W.; Qu, S. C.; Wang, Z. G. Synthesis of Shuttle-like ZnO Nanostructures from Precursor ZnS Nanoparticles. *Nanotechnology* **2005**, *16* (9), 1469–1473. https://doi.org/10.1088/0957-4484/16/9/008.

(40) Salavati-Niasari, M.; Davar, F.; Khansari, A. Nanospherical and Nanobundles of ZnO: Synthesis and Characterization. *J. Alloys Compd.* **2011**, *509* (1), 61–65. https://doi.org/10.1016/j.jallcom.2010.08.060.

(41) Stambolova, I.; Blaskov, V.; Shipochka, M.; Vassilev, S.; Dushkin, C.; Dimitriev, Y. Porous Photocatalytically Active ZnO Films Obtained from Ethylcellulose Modified Solutions by Spray Pyrolysis. *Mater. Chem. Phys.* **2010**, *121* (3), 447–452. https://doi.org/10.1016/j.matchemphys.2010.02.004.

(42) Ullah Awan, S.; Hasanain, S. K.; Bertino, M. F.; Hassnain Jaffari, G. Ferromagnetism in Li Doped ZnO Nanoparticles: The Role of Interstitial Li. *J. Appl. Phys.* **2012**, *112* (10). https://doi.org/10.1063/1.4767364.

(43) Wahab, R.; Hwang, I. H.; Kim, Y.-S.; Musarrat, J.; Siddiqui, M. A.; Seo, H.-K.; Tripathy, S. K.; Shin, H.-S. Non-Hydrolytic Synthesis and Photo-Catalytic Studies of ZnO Nanoparticles. *Chem. Eng. J.* **2011**, *175*, 450–457. https://doi.org/10.1016/j.cej.2011.09.055.

(44) Winiarski, J.; Tylus, W.; Szczygieł, B. EIS and XPS Investigations on the Corrosion Mechanism of Ternary Zn–Co–Mo Alloy Coatings in NaCl Solution. *Appl. Surf. Sci.* **2016**, *364*, 455–466. https://doi.org/10.1016/j.apsusc.2015.12.183.

(45) Zhang, J.; Gao, D.; Yang, G.; Zhang, J.; Shi, Z.; Zhang, Z.; Zhu, Z.; Xue, D. Synthesis and Magnetic Properties of Zr Doped ZnO Nanoparticles. *Nanoscale Res. Lett.* **2011**, *6* (1), 587. https://doi.org/10.1186/1556-276X-6-587.